

Geophysical Research Letters

RESEARCH LETTER

10.1029/2020GL091943

Key Points:

- Highly productive subsurface diatom hotspots were observed on the Mid-Atlantic Bight continental slope in July 2019
- The hotspots were associated with the temperature-salinity signature of Gulf Stream (GS) water
- The hotspots appear to have resulted from the onshore intrusion and upwelling of GS water from a GS meander

Supporting Information:

Supporting Information may be found in the online version of this article.

Correspondence to:

H. Oliver,
holiver@whoi.edu












Citation:

Oliver, H., Zhang, W. G., Smith, W. O., Alatalo, P., Chappell, P. D., Hirzel, A. J., et al. (2021). Diatom hotspots driven by western boundary current instability. *Geophysical Research Letters*, 48, e2020GL091943. <https://doi.org/10.1029/2020GL091943>

Received 3 DEC 2020
 Accepted 22 MAR 2021

© 2021. American Geophysical Union.
 All Rights Reserved.

Diatom Hotspots Driven by Western Boundary Current Instability

Hilde Oliver¹ , Weifeng G. Zhang¹ , Walker O. Smith Jr.^{2,3} , Philip Alatalo¹ , P. Dreux Chappell⁴ , Andrew J. Hirzel¹ , Corday R. Selden⁴ , Heidi M. Sosik¹ , Rachel H. R. Stanley⁵ , Yifan Zhu⁴ , and Dennis J. McGillicuddy Jr.¹ 

¹Woods Hole Oceanographic Institution, Woods Hole, MA, USA, ²Virginia Institute of Marine Science, College of William & Mary, Gloucester Point, VA, USA, ³School of Oceanography, Shanghai Jiao Tong University, Shanghai, People's Republic of China, ⁴Department of Ocean and Earth Sciences, Old Dominion University, Norfolk, VA, USA, ⁵Department of Chemistry, Wellesley College, Wellesley, MA, USA

Abstract Climatic changes have decreased the stability of the Gulf Stream (GS), increasing the frequency at which its meanders interact with the Mid-Atlantic Bight (MAB) continental shelf and slope region. These intrusions are thought to suppress biological productivity by transporting low-nutrient water to the otherwise productive shelf edge region. Here we present evidence of widespread, anomalously intense subsurface diatom hotspots in the MAB slope sea that likely resulted from a GS intrusion in July 2019. The hotspots (at ~50 m) were associated with water mass properties characteristic of GS water (~100 m); it is probable that the hotspots resulted from the upwelling of GS water during its transport into the slope sea, likely by a GS meander directly intruding onto the continental slope east of where the hotspots were observed. Further work is required to unravel how increasingly frequent direct GS intrusions could influence MAB marine ecosystems.

Plain Language Summary As the climate has warmed, the changing large-scale circulation of the northwest Atlantic has resulted in increasing western boundary current instability. As a consequence, onshore intrusions of Gulf Stream (GS) water into the Northeast U.S. continental shelf have become increasingly frequent. The impacts of this shift on marine ecosystems have yet to be resolved. While these intrusions of low-nutrient GS water have been thought to potentially diminish biological productivity, we present evidence of an unexpectedly productive subsurface diatom bloom resulting from the direct intrusion of a GS meander toward the continental shelf. These results suggest that changing large-scale circulation has consequences for regional productivity that are not detectable by satellites by virtue of their occurrence well below the surface.

1. Introduction

The Mid-Atlantic Bight (MAB) region of the Northeast U.S. continental shelf is one of the world's most productive marine ecosystems (O'Reilly & Busch, 1984; O'Reilly et al., 1987) and is critical to regional commercial fisheries (Sherman et al., 1996). Unlike the MAB continental shelf and shelfbreak front (e.g., Ryan et al., 1999; Zhang et al., 2013), the MAB slope sea to the south is generally characterized by lower biomass (e.g., Xu et al., 2011), with summer subsurface chlorophyll (Chl) maximum layers dominated by nanoplankton (O'Reilly & Zetlin, 1998).

MAB net community production is highly sensitive to ocean circulation (Friedrichs et al., 2019), but the response of the region's marine ecosystems to recent changes in northwest Atlantic circulation remains poorly constrained. Over the past two decades, the destabilization point of the Gulf Stream (GS) has shifted westward, resulting in more vigorous meandering of the GS south of the MAB (Andres, 2016). Consequently, the influence of the GS on the MAB has increased through both direct intrusion of GS water (Gawarkiewicz et al., 2012) and indirect interactions associated with more frequent GS shedding of anticyclonic warm-core rings (WCRs) (Gangopadhyay et al., 2019; Gawarkiewicz et al., 2018). To first order, increasing intrusions of GS water have been expected to decrease slope sea biological productivity (e.g., Brown et al., 1985; Zhang & Gawarkiewicz, 2015) as surface GS water is more oligotrophic than the slope (Brown et al., 1985; Olson et al., 1994). Here, we show observations from the MAB slope sea suggesting that the opposite can also occur.

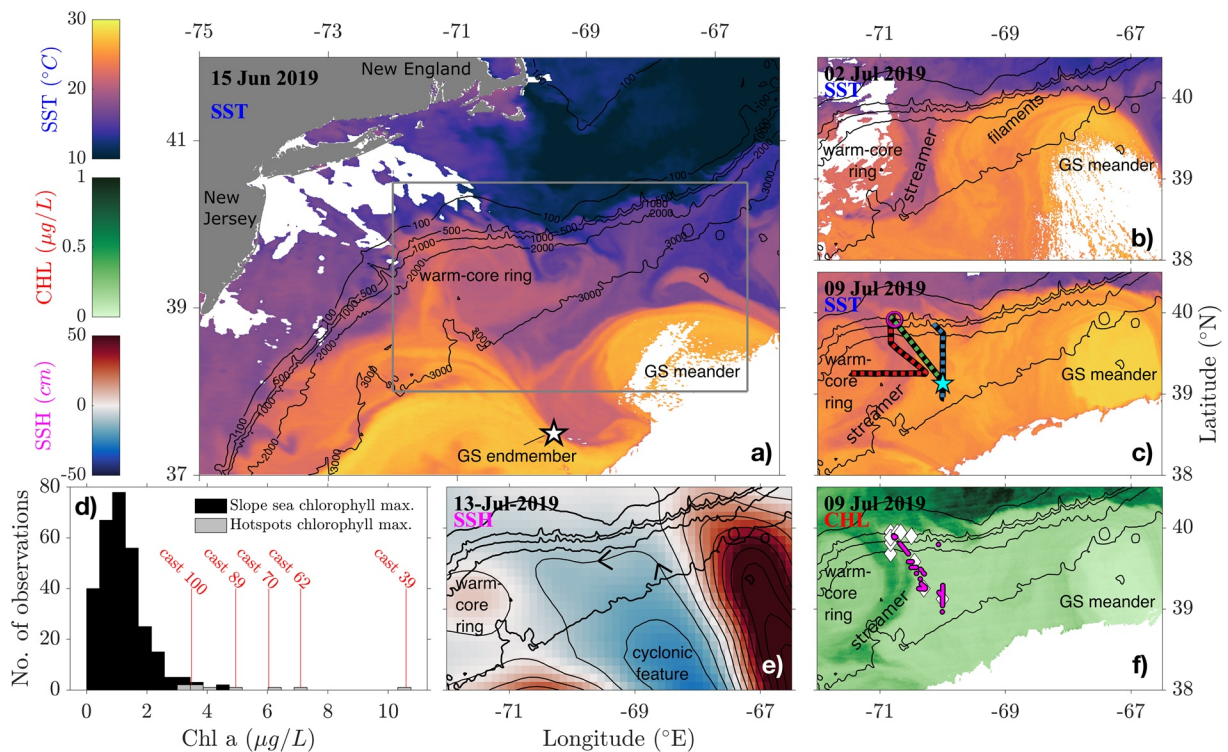


Figure 1. (a–c) Sea surface temperature (SST) showing the evolution of large-scale features in the Mid-Atlantic Bight (MAB) in the weeks leading up to TN368; (d) histogram of historical slope sea (depth > 200 m) chlorophyll (Chl) maxima measurements made from June–September from a MAB climatology (Zhang et al., 2013; Figure S1), including TN368 profiles (black bars), plotted with a histogram of TN368 hotspot Chl maximum concentrations (gray bars), with cast 100 and casts with Chl maxima > 4 $\mu\text{g/L}$ highlighted; (e) 7-day composite sea surface height (SSH) from Aviso+ with 10 cm contours; (f) VIIRS NOAA-20 1-day 1-km composite Chl during TN368. In (a), the white star shows location of the Gulf Stream (GS) endmember profile used to initialize the 1D model. In (c), striped lines indicate Video Plankton Recorder (VPR) tows 2 (red), 7 (blue), and 8 (green) shown in Figure 2; cyan star shows the location of station SLP (Cast 100), used for 1D model validation; magenta circle at the intersection of VPR tows 2 and 8 shows the location of REMUS mission 4a (at a much smaller scale). In (e), arrows on the cyclonic feature show a possible transport pathway of GS water to the edge of the shelf and hotspot region. In (f), white diamonds show locations of conductivity-temperature-depth casts at a hotspot, and magenta dots show locations of hotspots found by the VPR.

In July 2019, we observed unexpected diatom hotspots at the base of the euphotic zone in the slope sea with Chl concentrations several times higher than the climatological mean. We hypothesize that this feature resulted from the northward intrusion of a GS meander into the slope sea and was fueled by nutrients upwelled in GS water. Observatory data show occurrences of similar subsurface blooms in the slope sea in other recent years. Such widespread subsurface blooms of siliceous plankton may be important when considering the impacts of changing large-scale circulation patterns on MAB regional productivity.

Details of our methods are provided in Text S1–S12.

2. Subsurface Diatom Hotspots Found at High Salinities

In July 2019, the *R/V Thomas G. Thompson* cruise TN368 embarked to investigate the dynamics controlling primary productivity in the northern MAB shelfbreak region. In addition to traditional conductivity-temperature-depth (CTD) rosette sampling, high-resolution surveys of physical and biological properties in the upper water column (<100 m) were conducted with a Video Plankton Recorder (VPR) and autonomous underwater vehicle REMUS 600.

At the time of the cruise (July 6–18), a WCR was impinging on the MAB shelfbreak and entraining cooler shelf water at its periphery, drawing it into the warmer slope sea by its anticyclonic (clockwise) motion. This created a “streamer” of shelf water (e.g., Morgan & Bishop, 1977) at the eastern edge of the WCR (Figures 1b, 1c, and 1f). About 350 km to the east (at 67 W), a meander of the GS was transporting warmer

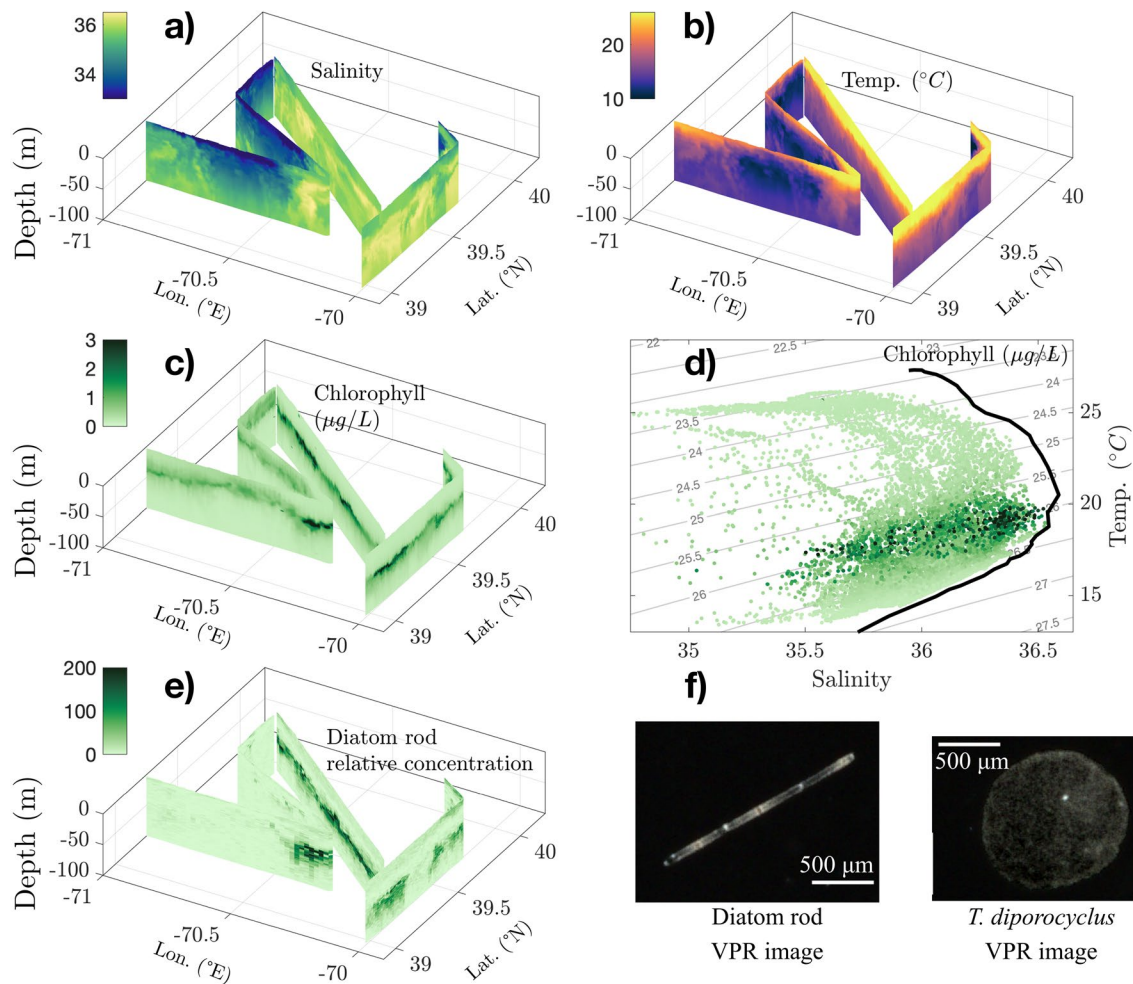


Figure 2. Video Plankton Recorder (VPR) tows 2, 7, and 8. (a) Salinity; (b) temperature; (c) chlorophyll (Chl) concentration; (d) corresponding T-S diagram from the tows, colored by Chl concentration, with the black line showing the Gulf Stream T-S profile from 69.5 E, 37 N from 1/10 summer objectively analyzed climatological means from the National Centers for Environmental Information Northwest Atlantic Regional Ocean Climatology, with the same Chl color bar used in (c); (e) relative diatom rod concentration; (f) two example VPR images: one classified as a “diatom rod,” the other a *T. diporocyclus* diatom colony.

GS water northward toward the shelfbreak. During the weeks preceding sampling, the WCR was migrating westward (e.g. Nof, 1983), while the meander was traveling eastward. In the broadening area between these anticyclonic features, satellite altimetry revealed a cyclonic (counterclockwise) feature (Figure 1e).

Directly east of the streamer, unexpected Chl hotspots were detected at ca. 50 m below the surface (Figure 2). These subsurface features were found in the oligotrophic slope sea east of the WCR in the following locations: (a) A narrow band on the eastern edge of the shelf water streamer, (b) along the offshore edge of the shelfbreak, and (c) within the cyclonic feature between the WCR and the GS meander (Figures 1e and 1f). We encountered hotspots at ~1/3 of all VPR profiles in the slope sea east of the WCR (Figure 4, VPR tows 7 and 8). The hotspots occurred where salinities were greater than 35.6 (Figure 2). This high-salinity water associated with the hotspots had water mass properties of GS water typically found hundreds of kilometers south of the shelf-break and 50 m deeper in the water column (Figure S2). This GS water (salinity >35.6) was ubiquitous in the slope sea sampled during TN368: It was present within the top 50 m at >99% of all slope sea profiles (VPR tows 7 and 8).

The hotspots were highly anomalous compared to typical Chl levels in the slope sea. The hotspot Chl concentrations were 1.9–8.8 standard deviations greater than the mean slope sea climatological Chl maximum ($1.3 \pm 1.1 \mu\text{g L}^{-1}$), with 4/10 of the hotspot casts reaching a Chl maximum concentration greater than the

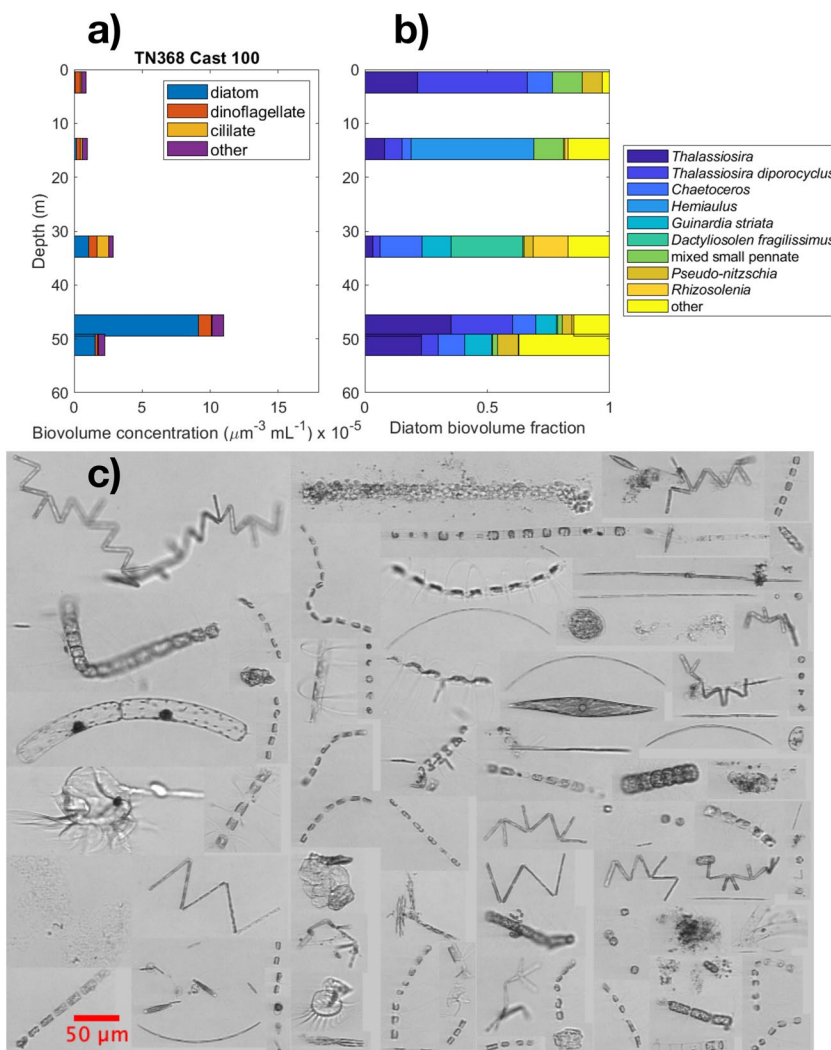


Figure 3. Imaging FlowCytobot (IFCB) classification and image subset from station SLP (Cast 100). (a) The relative biovolume of major phytoplankton groups at depths sampled; (b) the diatom taxa comprising the diatom assemblages in (a); (c) a collage of example IFCB images subset from 51 m depth.

highest summer slope sea Chl maximum documented in the World Ocean Database (Figure 1d). Usually, in oligotrophic waters, the depth of the Chl maximum tends to be decoupled from the maximum in phytoplankton biomass due to photoacclimation (Cullen, 2015; Fennel & Boss, 2003). The hotspots we observed bore high concentrations of particulate organic nitrogen and carbon, however, suggesting that they were high in biomass. They also corresponded to elevated biogenic silica concentrations and increased silicate drawdown relative to nitrate and ammonium, indicative of high diatom biomass (Figure S3).

Imaging FlowCytobot (IFCB) images affirmed that the plankton community within the Chl hotspots was dominated by diverse assemblages of diatoms (Figure 3). VPR image classification revealed that the Chl hotspots corresponded to large concentrations of rod-shaped diatoms (Figure 2e), as well as an abundance of colonial phytoplankton identified as *Thalassiosira* sp. from IFCB images. Accordingly, the diatom 18S rDNA pool at all hotspot sites was dominated (30%–73% relative abundance, Figure S5) by the mucilaginous, colony-forming diatom *Thalassiosira diporocyclus*, which has been previously observed in association with GS WCRs (Fryxell et al., 1984). Numerous centric diatoms and chain-forming, pennate diatoms were also present within the hotspots (Figure 3). *T. diporocyclus* was not observed on the shelf, but was present at lower relative abundance (~10%) in nonhotspot slope waters.

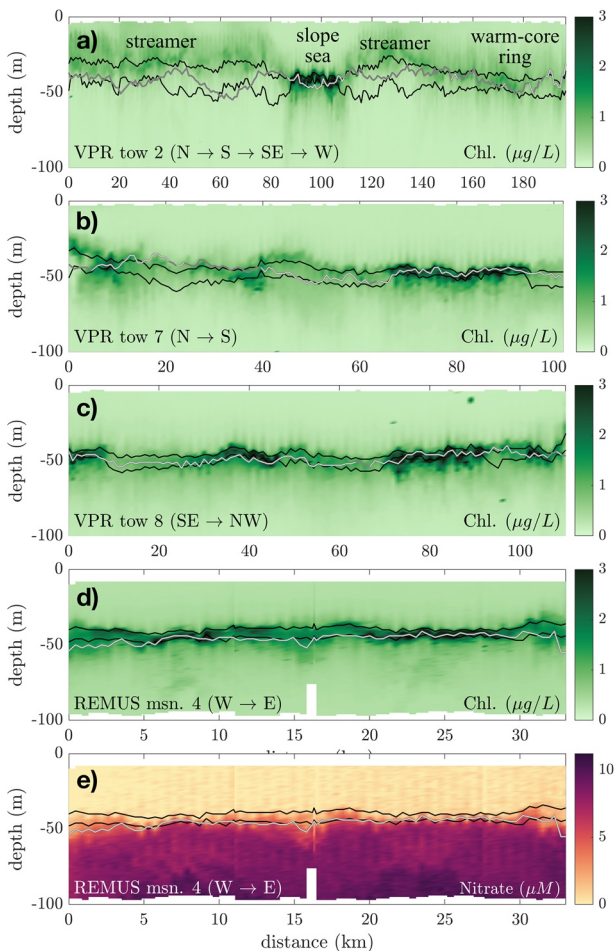


Figure 4. Video Plankton Recorder (a–c) and REMUS (d–e) transects plotted against distance, showing chlorophyll hotspots and elevated nitrate where the $\sigma_{\theta} = 26.0 \text{ kg m}^{-3}$ isopycnal receives adequate irradiance. $\sigma_{\theta} = 26.0 \text{ kg m}^{-3}$ isopycnal depth is plotted in white where salinity > 35.6 ; gray where fresher. The range of estimated euphotic depth (depth of 1% light, ± 1 standard deviation) is shown by black lines.

These diatom hotspots were acclimated to low irradiance levels, and defined by thin peaks of high primary productivity near the euphotic depth. While a depth-resolving bio-optical model (Behrenfeld & Falkowski, 1997a, 1997b) closely reproduced measured profiles of net productivity at hotspot casts, estimated integrated productivity from deck-board incubations was lower than modeled for hotspots, as the thin Chl maxima were usually missed by discrete water samples (Figure S6). This systematic underestimation of measured integrated productivity was much less for nonhotspot casts, where the bio-optical model slightly underestimated integrated productivity. Profiles of triple oxygen isotopes showed that the hotspots had higher levels of gross primary production than the surrounding waters (Figure S8). The estimated rate of hotspot gross primary production from triple oxygen isotopes at a depth a few meters below the peak Chl in cast 71 was $48 \text{ mg C m}^{-3} \text{ d}^{-1}$ — on the same order as estimated by the bio-optical model even though the estimate stems from a completely independent method that measures an integrated average of production in the hotspot over the preceding two weeks.

The deep diatom hotspots were consistently detected at the $\sigma_{\theta} = 26.0 \text{ kg m}^{-3}$ isopycnal (Figure 2d) east of the WCR where there was (a) high salinity water (> 35.6), and (b) sufficiently clear overlying water to allow for a deep ($\sim 50 \text{ m}$) subsurface bloom (Figure 4). High Chl could be found where the $\sigma_{\theta} = 26.0 \text{ kg m}^{-3}$ isopycnal rose above the euphotic depth (the depth of 1% surface irradiance levels), provided that the salinity at the $\sigma_{\theta} = 26.0 \text{ kg m}^{-3}$ isopycnal was also of deeper GS origin (> 35.6 , Figure 4). Within the cyclonic feature (VPR tows 7 and 8, Figure 4), the $\sigma_{\theta} = 26.0 \text{ kg m}^{-3}$ isopycnal was consistently close to 50 m and near the base of the euphotic zone. Vertical displacement of the isopycnal by only a few meters could therefore result in a hotspot. The higher-resolution REMUS 600 survey of the hotspot conducted on July 12–13 near the shelfbreak (Figure 4) included measurements from a Submersible Ultraviolet Nitrate Analyzer and confirmed elevated nitrate concentrations at the $\sigma_{\theta} = 26.0 \text{ kg m}^{-3}$ isopycnal. We note that these conditions only held east of the shelf water streamer; high salinity and high Chl hotspots were not detected within the WCR (Figure 4a).

3. Upwelling of Deep Gulf Stream Water

The slope sea hotspots were typically observed at $\sim 50 \text{ m}$. At the northern edge of the GS, however, the temperature-salinity signature associated with the slope sea hotspots occurs at $\sim 100 \text{ m}$, about 50 m deeper than observed in the slope sea (Figure 5). We propose that the upward transport of this deep GS water during its northward intrusion in the MAB slope sea supplied deeper nutrients to the base of the euphotic zone, driving subsurface hotspots.

We tested the plausibility that upwelling of GS water properties could reproduce observations of physical and biogeochemical properties, particularly the high Chl maximum value, at station SLP (Cast 100), the TN368 slope sea station (cyan star in Figure 1c). We applied an upward vertical velocity typical of submesoscale features in the region (e.g., Zhang & Partida, 2018) to characteristic GS profiles of temperature, salinity, and nutrients. This analysis was performed using a one-dimensional model (Price et al., 1986) of the upper ocean (0–150 m) coupled to a nitrate-phytoplankton-zooplankton-detritus biogeochemical model (modified from Fennel et al., 2006; Powell et al., 2006). The upward vertical velocity varied linearly with water depth, starting from zero at the sea surface. We applied a maximum vertical velocity at 150 m of 10^{-4} m s^{-1} ($\sim 6 \text{ m d}^{-1}$ at 150 m and $\sim 2 \text{ m d}^{-1}$ at 50 m). After 12 days, the model closely matched observations of temperature, salinity, nitrate, and Chl below the surface mixed layer at station SLP (Figure 5a), supporting the plausibility that the observed subsurface hotspots resulted from the upwelling of GS water

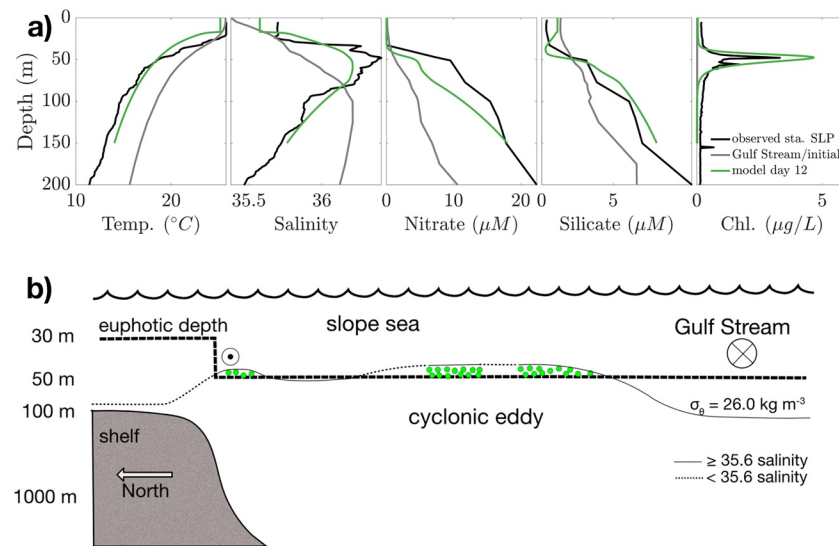


Figure 5. 1D and conceptual models of Gulf Stream water upwelling: (a) 1D model initial profiles (gray) and output at day 12 (green), versus observations from SLP (Cast 100; black); (b) north-south schematic of slope sea hotspots.

from south of the MAB, despite neglecting the horizontal advective mechanisms at play during its transport into the slope sea euphotic zone.

4. Discussion and Conclusions

4.1. Transport Pathways

Hotspot formation likely occurred shortly before the cruise. As the GS meander moved northeastward toward the shelfbreak, it carried filaments of warm GS water along its western edge (Figure 1b). These filaments may have been transported northward by the cyclonic feature formed in the slope sea (Lee et al., 1991, Figure 1e). This background cyclonic gyre typifies the MAB slope sea (Csanady & Hamilton, 1988), with the density surface $\sigma_\theta = 26.0 \text{ kg m}^{-3}$ doming to the base of the euphotic zone ($\sim 50 \text{ m}$) in summer regional climatologies of the Northwest Atlantic (Seidov, 2016). Isopycnals are known to shoal at the northern edges of anticyclonic meanders (Bower & Rossby, 1989), transporting nutrients into the euphotic zone and stimulating phytoplankton growth (Flierl & Davis, 1993). Upwelling may also have occurred in a divergent flow at the western meander edge (e.g., Hitchcock et al., 1993; Olson et al., 1994). It is thus plausible that GS water was vertically transported along isopycnals and into the euphotic zone during its northward transport by the slope sea cyclonic feature, though a high-resolution 3D model is required to determine the actual driving mechanism(s).

Surface GS waters are oligotrophic and nutrient-poor; however, nutrient concentrations at depth are greater within the GS relative to the waters of the same isopycnals in the slope sea (Csanady, 1990; Palter & Lozier, 2008; Pelegri & Csanady, 1991). Schollaert et al. (2004) suggested the flux of nutrient-rich subsurface waters of the GS could explain interannual variability in the magnitude of the spring bloom in the slope sea; our study shows nutrient supply from the GS influences subsurface summer productivity. Hotspots within the slope sea were generally found where there was slight uplift of the $\sigma_\theta = 26.0 \text{ kg m}^{-3}$ isopycnal into the photic zone (Figures 4a and 4b), which may have driven episodic new production (e.g., Goldman, 1988). Observed water mass characteristics suggest interleaving of slope and GS waters. We thus propose both slope and GS waters were upwelled by isopycnal doming by the cyclonic eddy (Figure 5b; Yoder et al., 1981). Hotspots occurred only in those places where the subsurface GS waters (salinity > 35.6) were sufficiently upwelled to be illuminated (Figure 5). Deformation or stretching of the filaments of GS water generated from baroclinic instability at the meander edge (Figures 1b and 1c) may have also resulted in GS/slope water frontogenesis (Mied et al., 1996; Zhang & Partida, 2018). The associated upward velocities may have

enhanced or driven the increased illumination of the nutrient-rich $\sigma_{\theta} = 26.0 \text{ kg m}^{-3}$ isopycnal (e.g., Lévy et al., 2001; Mahadevan, 2016).

Subsurface Chl hotspots were also observed at the shelf/slope water interface, which was found near the shelfbreak and at the eastern streamer edge. At the shelf/slope water interface the euphotic depth shoals with the transition from clear slope water to turbid shelf water (Figure 4). Consequently, while under shelf water the $\sigma_{\theta} = 26.0 \text{ kg m}^{-3}$ isopycnal does not receive adequate photosynthetically active radiation to support significant phytoplankton growth (Figure 5b). The hotspots at the streamer edge (Figure 4, VPR transect 2) may have originated near the shelfbreak before being advected southward by the anticyclonic currents at the edge of the WCR along with the shelf water streamer.

4.2. Implications

The anomalous subsurface diatom hotspots reached from the shelf edge to the southern and eastern boundaries of our sampling area, and the GS water associated with the hotspots was present in the top 50 m at >99% of VPR slope profiles (Figure 2). It is therefore probable that our snapshot observations did not capture the full extent of the diatom hotspots in the slope sea. The hotspots were anomalous relative to the summer slope sea Chl climatology, but similar high-salinity, high-Chl events may not be uncommon in the region: Such events were recorded by summer glider measurements from the Ocean Observatories Initiative (OOI) Pioneer Array (Trowbridge et al., 2019) in three of the past 5 years in the MAB slope sea (Figure S10). During the 2 years where such an event was not captured by gliders (2017 and 2018), the shelfbreak front extended south of the glider area, and slope water was not measured. High-salinity, high-Chl events could still have occurred in the slope sea during these periods. A shoaling nutricline giving rise to episodic diatom-dominated new production at low light has also been well documented in other parts of the ocean (e.g., Goldman, 1988; Goldman & McGillicuddy, 2003); our observations suggest this potential mechanism in the MAB slope sea corresponded with the intrusion of GS water. Given that GS intrusions have become more frequent and persistent in recent decades, these subsurface hotspots may be important when considering the integrated effects of changing North Atlantic circulation on regional ecosystems and carbon export.

Western boundary current systems worldwide have shown shifting trends. For example, increasing instability has been documented for the East Australian Current (Sloyan et al., 2016) and Agulhas Current (Beal & Elipot, 2016), and the Kuroshio Extension undergoes decadal shifts between stable and unstable states (Qiu & Chen, 2010). To understand the influence of changing western boundary currents on marine ecosystems, we must unravel the mechanisms by which meanders, WCRs, and other intrusions influence light and nutrient conditions for both surface and subsurface phytoplankton growth. Assessing the long-term trajectory of primary productivity with respect to an increasingly meandering western boundary current will require a deeper mechanistic understanding of the phenomena described in this study, for which further and persistent subsurface observations and process-oriented coupled physical-biogeochemical modeling are needed. Continued monitoring of the slope sea by the OOI Pioneer Array offshore moorings, gliders, and autonomous underwater vehicles will be key to achieving this understanding. Finally, this study highlights the potential for disparate regional impacts of changing large-scale circulation on marine ecosystems: Whereas our findings suggests that direct interaction of the GS with the continental shelf and slope could drive enhanced productivity at the Chl maximum in the subtropical Atlantic, a slower nutrient stream could suppress subarctic primary productivity in future climate scenarios (Whitt & Jansen, 2020).

Data Availability Statement

All CTD, VPR, and bottle fields are archived at the SPIROPA project page at the Biological & Chemical Oceanography Data Management Office (BCO-DMO) with DOIs 10.26008/1912/bco-dmo.807119.2, 10.26008/1912/bco-dmo.848898.1, and 10.26008/1912/bco-dmo.849340.1. SPIROPA IFCB images are available at <https://ifcb-data.whoi.edu/timeline?dataset=SPIROPA>. Amplicon sequence variants read counts are included in Data-set S1.

Acknowledgments

This research was supported by the National Science Foundation (OCE-1657803 and OCE-1657855) and the Dalio Explorer Fund. H. Oliver was supported by a WHOI Postdoctoral Scholar award. We thank Jeff Turner and Christy Petitpas for their work on higher trophic levels, Fred Thwaites and Josh Eaton for VPR operations, Mike Purcell, Gwyneth Packard, and Judson Poole for REMUS surveys, Taylor Crockford for IFCB operations, Emily Peacock for contributing to IFCB image classification, Meredith Meyer for contributions to productivity data analysis, Frannie Adams, Lumi Kinjo, Erin Kim, and Zoe Sandwith for contributing to triple oxygen isotope data collection and analysis, and Sophie Clayton for her thoughts on our modeling approach, as well as our SPIROPA colleagues and crew of the *R/V Thomas G. Thompson* for their assistance and support at sea.

References

Andres, M. (2016). On the recent destabilization of the Gulf Stream path downstream of Cape Hatteras. *Geophysical Research Letters*, 43(18), 9836–9842. <https://doi.org/10.1002/2016GL069966>

Beal, L. M., & Elipot, S. (2016). Broadening not strengthening of the Agulhas Current since the early 1990s. *Nature*, 540(7634), 570–573. <https://doi.org/10.1038/nature19853>

Behrenfeld, M. J., & Falkowski, P. G. (1997a). A consumer's guide to phytoplankton primary productivity models. *Limnology and Oceanography*, 42(7), 1479–1491. <https://doi.org/10.4319/lo.1997.42.7.1479>

Behrenfeld, M. J., & Falkowski, P. G. (1997b). Photosynthetic rates derived from satellite-based chlorophyll concentration. *Limnology and Oceanography*, 42(1), 1–20. <https://doi.org/10.4319/lo.1997.42.1.0001>

Bower, A. S., & Rossby, T. (1989). Evidence of cross-frontal exchange processes in the Gulf Stream based on isopycnal RAFOS float data. *Journal of Physical Oceanography*, 19(9), 1177–1190. [https://doi.org/10.1175/1520-0485\(1989\)019<1177:eocfep>2.0.co;2](https://doi.org/10.1175/1520-0485(1989)019<1177:eocfep>2.0.co;2)

Brown, O. B., Evans, R. H., Brown, J. W., Gordon, H. R., Smith, R. C., & Baker, K. S. (1985). Phytoplankton blooming off the U.S. East coast: A satellite description. *Science*, 229(4709), 163–167. <https://doi.org/10.1126/science.229.4709.163>

Csanady, G. T. (1990). Physical basis of coastal productivity: The SEEP and MASAR experiments. *Eos, Transactions American Geophysical Union*, 71(36), 1060–1065. <https://doi.org/10.1029/EO071i036p1060>

Csanady, G. T., & Hamilton, P. (1988). Circulation of slopewater. *Continental Shelf Research*, 8(5-7), 565–624. [http://dx.doi.org/10.1016/0278-4343\(88\)90068-4](http://dx.doi.org/10.1016/0278-4343(88)90068-4)

Cullen, J. J. (2015). Subsurface chlorophyll maximum layers: Enduring enigma or mystery solved? *Annual Review of Marine Science*, 7(1), 207–239. <https://doi.org/10.1146/annurev-marine-010213-135111>

Fennel, K., & Boss, E. (2003). Subsurface maxima of phytoplankton and chlorophyll: Steady-state solutions from a simple model. *Limnology and Oceanography*, 48(4), 1521–1534. <https://doi.org/10.4319/lo.2003.48.4.1521>

Fennel, K., Wilkin, J., Levin, J., Moisan, J., O'Reilly, J., & Haidvogel, D. (2006). Nitrogen cycling in the Middle Atlantic Bight: Results from a three-dimensional model and implications for the North Atlantic nitrogen budget. *Global Biogeochemical Cycles*, 20(3), 1–14. <https://doi.org/10.1029/2005GB002456>

Flierl, G. R., & Davis, C. S. (1993). Biological effects of Gulf Stream meandering. *Journal of Marine Research*, 51(3), 529–560. <https://doi.org/10.1357/0022240933224016>

Friedrichs, M. A. M., St-Laurent, P., Xiao, Y., Hofmann, E., Hyde, K., Mannino, A., et al. (2019). Ocean circulation causes strong variability in the Mid-Atlantic Bight nitrogen budget. *Journal of Geophysical Research: Oceans*, 124, 113–134. <https://doi.org/10.1029/2018JC014424>

Fryxell, G. A., Gould, R. W., & Watkins, T. P. (1984). Gelatinous colonies of the diatom *Thalassiosira* in Gulf Stream Warm Core Rings including *T. fragilis*, sp. nov. *British Phycological Journal*, 19(2), 141–156. <https://doi.org/10.1080/00071618400650151>

Gangopadhyay, A., Gawarkiewicz, G., Silva, E. N. S., Monim, M., & Clark, J. (2019). An observed regime shift in the formation of warm core rings from the Gulf Stream. *Scientific Reports*, 9(1), 1–9. <https://doi.org/10.1038/s41598-019-48661-9>

Gawarkiewicz, G., Todd, R. E., Zhang, W., Partida, J., Gangopadhyay, A., Monim, M. U. H., et al. (2018). The changing nature of shelf-break exchange revealed by the OOI Pioneer Array. *Oceanography*, 31(1), 60–70. <https://doi.org/10.5670/oceanog.2018.110>

Gawarkiewicz, G. G., Todd, R. E., Plueddemann, A. J., Andres, M., & Manning, J. P. (2012). Direct interaction between the Gulf Stream and the shelfbreak south of New England. *Scientific Reports*, 2(1), 553. <https://doi.org/10.1038/srep00553>

Goldman, J. C. (1988). Spatial and Temporal Discontinuities of Biological Processes in Pelagic Surface Waters. In B. J. Rothschild (Ed.), *Toward a Theory on Biological-Physical Interactions in the World Ocean* (pp. 273–296). Dordrecht: Springer Netherlands. https://doi.org/10.1007/978-94-009-3023-0_15

Goldman, J. C., & McGillicuddy, D. J. (2003). Effect of large marine diatoms growing at low light on episodic new production. *Limnology and Oceanography*, 48(3), 1176–1182. <https://doi.org/10.4319/lo.2003.48.3.1176>

Hitchcock, G. L., Mariano, A. J., & Rossby, T. (1993). Mesoscale pigment fields in the Gulf Stream: Observations in a meander crest and trough. *Journal of Geophysical Research*, 98(5), 8425–8445. <https://doi.org/10.1029/92jc02911>

Lee, T. N., Yoder, J. A., & Atkinson, L. P. (1991). Gulf Stream frontal eddy influence on productivity of the southeast US Continental Shelf. *Journal of Geophysical Research*, 96(C12), 191–205. <https://doi.org/10.1029/91jc02450>

Lévy, M., Klein, P., & Treguier, A. M. (2001). Impact of sub-mesoscale physics on production and subduction of phytoplankton in an oligotrophic regime. *Journal of Marine Research*, 59(4), 535–565. <https://doi.org/10.1357/002224001762842181>

Mahadevan, A. (2016). The impact of submesoscale Physics on primary productivity of plankton. *Annual Review of Marine Science*, 8(1), 161–184. <https://doi.org/10.1146/annurev-marine-010814-015912>

Mied, R. P., Shen, C. Y., Evans, T. E., & Lindemann, G. J. (1996). Frontogenesis with ageostrophic vertical shears and horizontal density gradients: Gulf Stream meanders onto the continental shelf. *Journal of Geophysical Research*, 101(C8), 18079–18104. <https://doi.org/10.1029/96JC01423>

Morgan, C. W., & Bishop, J. M. (1977). An example of gulf stream eddy-induced water exchange in the Mid-Atlantic Bight. *Journal of Physical Oceanography*, 7, 472–479. [https://doi.org/10.1175/1520-0485\(1977\)007<0472:AEOGSE>2.0.CO;2](https://doi.org/10.1175/1520-0485(1977)007<0472:AEOGSE>2.0.CO;2)

Nof, D. (1983). On the migration of isolated eddies with application to Gulf Stream rings. *Journal of Marine Research*, 41(3), 399–425. <https://doi.org/10.1357/002224083788519687>

Olson, D., Hitchcock, G., Mariano, A., Ashjian, C., Peng, G., Nero, R., & Podesta, G. (1994). Life on the edge: Marine life and fronts. *Oceanography*, 7(2), 52–60. <https://doi.org/10.5670/oceanog.1994.03>

O'Reilly, J. E., & Busch, D. A. (1984). Phytoplankton primary production on the northwestern Atlantic shelf. *Rapports et Proces-Verbaux des Reunions Conseil International pour l'Exploration de la Mer*, 183, 255–268.

O'Reilly, J. E., Evans-Zetlin, C., & Busch, D. A. (1987). Primary production. In R. H. Backus, & D. W. Bourne (Eds.), *Georges bank* (p. 220–233). Cambridge, MA: MIT Press.

O'Reilly, J. E., & Zetlin, C. (1998). *Season, horizontal, and vertical distribution of phytoplankton chlorophyll a in the northeast U.S. continental shelf ecosystem*, NOAA Technical Rep. NMFS, 139, (pp. 119). Seattle, Washington: NOAA, US Department of Commerce.

Palter, J. B., & Lozier, M. S. (2008). On the source of Gulf Stream nutrients. *Journal of Geophysical Research*, 113, C06018. <https://doi.org/10.1029/2007JC004611>

Pelegri, J. L., & Csanady, G. T. (1991). Nutrient transport and mixing in the gulf stream. *Journal of Geophysical Research*, 96(C2), 2577–2583. <https://doi.org/10.1029/90JC02535>

Powell, T. M., Lewis, C. V. W. W., Curchitser, E. N., Haidvogel, D. B., Hermann, A. J., & Dobbins, E. L. (2006). Results from a three-dimensional, nested biological-physical model of the California Current System and comparisons with statistics from satellite imagery. *Journal of Geophysical Research*, 111, 1–14. <https://doi.org/10.1029/2004JC002506>

- Price, J. F., Weller, R. A., & Pinkel, R. (1986). Diurnal cycling: Observations and models of the upper ocean response to diurnal heating, cooling, and wind mixing. *Journal of Geophysical Research*, *91*(C7), 8411–8427. <https://doi.org/10.1029/JC091iC07p08411>
- Qiu, B., & Chen, S. (2010). Eddy-mean flow interaction in the decadal modulating Kuroshio Extension system. *Deep Sea Research Part II: Topical Studies in Oceanography*, *57*(13–14), 1098–1110. <https://doi.org/10.1016/j.dsr2.2008.11.036>
- Ryan, J. P., Yoder, J. A., & Cornillon, P. C. (1999). Enhanced chlorophyll at the shelfbreak of the Mid-Atlantic Bight and Georges Bank during the spring transition. *Limnology and Oceanography*, *44*(1), 1–11. <https://doi.org/10.4319/lo.1999.44.1.0001>
- Schollaert, S. E., Rossby, T., & Yoder, J. A. (2004). Gulf Stream cross-frontal exchange: Possible mechanisms to explain interannual variations in phytoplankton chlorophyll in the Slope Sea during the SeaWiFS years. *Deep Sea Research Part II: Topical Studies in Oceanography*, *51*(1), 173–188. <https://doi.org/10.1016/j.dsr2.2003.07.017>
- Seidov, D., Baranova, O. K., Boyer, T. P., Cross, S. L., Mishonov, A. V., & Parsons, A. R. (2016). *Northwest Atlantic Regional Climatology (NCEI Accession 0155889)* (pp. 1–56). NOAA National Centers for Environmental Information. <https://doi.org/10.7289/v5rf5s2q>
- Sherman, K., Jaworski, N. A., & Smayda, T. J. (1996). *The Northeast shelf ecosystem: Assessment, sustainability and management*. Cambridge, MA, USA. Blackwell Science, Inc.
- Sloyan, B. M., Ridgway, K. R., & Cowley, R. (2016). The East Australian Current and property transport at 27°S from 2012 to 2013. *Journal of Physical Oceanography*, *46*(3), 993–1008. <https://doi.org/10.1175/JPO-D-15-0052.1>
- Trowbridge, J., Weller, R., Kelley, D., Dever, E., Plueddemann, A., Barth, J. A., & Kawka, O. (2019). The ocean observatories initiative. *Frontiers in Marine Science*, *6*(MAR), 1–23. <https://doi.org/10.3389/fmars.2019.00074>
- Whitt, D. B., & Jansen, M. F. (2020). Slower nutrient stream suppresses Subarctic Atlantic Ocean biological productivity in global warming. *Proceedings of the National Academy of Sciences of the United States of America*, *117*(27), 15504–15510. <https://doi.org/10.1073/pnas.2000851117>
- Xu, Y., Chant, R., Gong, D., Castelao, R., Glenn, S., & Schofield, O. (2011). Seasonal variability of chlorophyll a in the Mid-Atlantic Bight. *Continental Shelf Research*, *31*(16), 1640–1650. <https://doi.org/10.1016/j.csr.2011.05.019>
- Yoder, J. A., Atkinson, L. P., Lee, T. N., Kim, H. H., & McClain, C. R. (1981). Role of Gulf Stream frontal eddies in forming phytoplankton patches on the outer southeastern shelf. *Limnology and Oceanography*, *26*(6), 1103–1110. <https://doi.org/10.4319/lo.1981.26.6.1103>
- Zhang, W. G., & Gawarkiewicz, G. G. (2015). Dynamics of the direct intrusion of Gulf Stream ring water onto the Mid-Atlantic Bight shelf. *Geophysical Research Letters*, *42*, 7687–7695. <https://doi.org/10.1002/2015GL065530>
- Zhang, W. G., McGillicuddy, D. J., & Gawarkiewicz, G. G. (2013). Is biological productivity enhanced at the New England shelfbreak front? *Journal of Geophysical Research: Oceans*, *118*, 517–535. <https://doi.org/10.1002/jgrc.20068>
- Zhang, W. G., & Partida, J. (2018). Frontal subduction of the Mid-Atlantic Bight Shelf Water at the onshore edge of a warm-core ring. *Journal of Geophysical Research: Oceans*, *123*, 7795–7818. <https://doi.org/10.1029/2018JC013794>

References From the Supporting Information

- Altschul, S. F., Gish, W., Miller, W., Myers, E. W., & Lipman, D. J. (1990). Basic local alignment search tool. *Journal of Molecular Biology*, *215*(3), 403–410. [https://doi.org/10.1016/S0022-2836\(05\)80360-2](https://doi.org/10.1016/S0022-2836(05)80360-2)
- Bray, J. R., & Curtis, J. T. (1957). An ordination of the upland forest communities of Southern Wisconsin. *Ecological Monographs*, *27*(4), 325–349. <https://doi.org/10.2307/1942268>
- Brzezinski, M. A. (2004). The Si:C:N Ratio of Marine Diatoms: Interspecific Variability and the Effect of some Environmental Variables. *Journal of Phycology*, *21*(3), 347–357. <https://doi.org/10.1111/j.0022-3646.1985.00347.x>
- Callahan, B. J., McMurdie, P. J., Rosen, M. J., Han, A. W., Johnson, A. J. A., & Holmes, S. P. (2016). DADA2: High-resolution sample inference from Illumina amplicon data. *Nature Methods*, *13*(7), 581–583. <https://doi.org/10.1038/nmeth.3869>
- Chappell, P. D., Virginia Armbrust, E., Barbeau, K. A., Bundy, R. M., Moffett, J. W., Vedamati, J., & Jenkins, B. D. (2019). Patterns of diatom diversity correlate with dissolved trace metal concentrations and longitudinal position in the northeast Pacific coastal–offshore transition zone. *Marine Ecology Progress Series*, *609*, 69–86. <https://doi.org/10.3354/meps12810>
- Clarke, K. R., & Gorley, R. N. (2018). *Getting started with PRIMER v7. Primer-E, (1)*, 20. <https://doi.org/10.22201/ib.20078706e.2018.3.2409>
- Davis, C. S., Thwaites, F. T., Gallagher, S. M., Hu, Q., Naiman, M., Sutton, T., et al. (2005). A three-axis fast-tow digital Video Plankton Recorder for rapid surveys of plankton taxa and hydrography. *Limnology and Oceanography*, *3*, 59–74. <https://doi.org/10.4319/lo.2005.3.59>
- Fasham, M. J. R., Ducklow, H. W., & McKelvie, S. M. (1990). A nitrogen-based model of plankton dynamics in the oceanic mixed layer. *Journal of Marine Research*, *48*(3), 591–639. <https://doi.org/10.1357/002224090784984678>
- Friedrichs, M. A. M., Carr, M. E., Barber, R. T., Scardi, M., Antoine, D., Armstrong, R. A., et al. (2009). Assessing the uncertainties of model estimates of primary productivity in the tropical Pacific Ocean. *Journal of Marine Systems*, *76*(1–2), 113–133. <https://doi.org/10.1016/j.jmarsys.2008.05.010>
- García, H., Weathers, K. W., Paver, C. R., Smolyar, I., Boyer, T. P., Locarnini, R. A., et al. (2019). *World Ocean Atlas 2018. Vol. 4: Dissolved inorganic nutrients (phosphate, nitrate and nitrate+nitrite, silicate)*. NOAA Atlas NESDIS 82, 4(July) (p. 35).
- González, P., Castaño, A., Peacock, E. E., Díez, J., del Coz, J. J., & Sosik, H. M. (2019). Automatic plankton quantification using deep features. *Journal of Plankton Research*, *41*(4), 449–463. <https://doi.org/10.1093/plankt/fbz023>
- Hendricks, M. B., Bender, M. L., & Barnett, B. A. (2004). Net and gross O₂ production in the Southern Ocean from measurements of biological O₂ saturation and its triple isotope composition. *Deep-Sea Research Part I: Oceanographic Research Papers*, *51*(11), 1541–1561. <https://doi.org/10.1016/j.dsr.2004.06.006>
- Holmes, R. M., Aminot, A., Kéruef, R., Hooker, B. A., & Peterson, B. J. (1999). A simple and precise method for measuring ammonium in marine and freshwater ecosystems. *Canadian Journal of Fisheries and Aquatic Sciences*, *56*(10), 1801–1808. <https://doi.org/10.1139/f99-128>
- Jassby, A. D., & Platt, T. (1976). Mathematical formulation of the relationship between photosynthesis and light for phytoplankton. *Limnology and Oceanography*, *21*(4), 540–547. <https://doi.org/10.4319/lo.1976.21.4.0540>
- Joyce, T. M., Deser, C., & Spall, M. A. (2000). The relation between decadal variability of subtropical mode water and the North Atlantic Oscillation. *Journal of Climate*, *13*(14), 2550–2569. [https://doi.org/10.1175/1520-0442\(2000\)013<2550:TRBDVO>2.0.CO;2](https://doi.org/10.1175/1520-0442(2000)013<2550:TRBDVO>2.0.CO;2)
- Juranek, L. W., & Quay, P. D. (2013). Using triple isotopes of dissolved oxygen to evaluate global marine productivity. *Annual Review of Marine Science*, *5*(1), 503–524. <https://doi.org/10.1146/annurev-marine-121211-172430>
- Kaiser, J. (2011). Technical note: Consistent calculation of aquatic gross production from oxygen triple isotope measurements. *Biogeochemistry*, *8*(7), 1793–1811. <https://doi.org/10.5194/bg-8-1793-2011>

- Kalnay, E., Kanamitsu, M., Kistler, R., Collins, W., Deaven, D., Gandin, L., et al. (1996). The NCEP/NCAR 40-year reanalysis project. *Bulletin of the American Meteorological Society*, 77(3), 437–471. [https://doi.org/10.1175/1520-0477\(1996\)077<0437:tnyrp>2.0.co;2](https://doi.org/10.1175/1520-0477(1996)077<0437:tnyrp>2.0.co;2)
- Luz, B., & Barkan, E. (2000). Assessment of oceanic productivity with the triple-isotope composition of dissolved oxygen. *Science*, 288(5473), 2028–2031. <https://doi.org/10.1126/science.288.5473.2028>
- Luz, B., & Barkan, E. (2005). The isotopic ratios $^{17}\text{O}/^{16}\text{O}$ and $^{18}\text{O}/^{16}\text{O}$ in molecular oxygen and their significance in biogeochemistry. *Geochimica et Cosmochimica Acta*, 69(5), 1099–1110. <https://doi.org/10.1016/j.gca.2004.09.001>
- Martin, M. (2011). Cutadapt removes adapter sequences from high-throughput sequencing reads. *EMBnet Journal*, 17(1), 10–12. <https://doi.org/10.14806/ej.17.1.200>
- Moberg, E. A., & Sosik, H. M. (2012). Distance maps to estimate cell volume from two-dimensional plankton images. *Limnology and Oceanography*, 10(4), 278–288. <https://doi.org/10.4319/lom.2012.10.278>
- Morel, A. (1974). Optical properties of pure water and pure sea water. *Optical Aspects of Oceanography*, 1, 1–24.
- Platt, T., & Jassby, A. D. (1976). The relationship between photosynthesis and light for natural assemblages of coastal marine phytoplankton. *Journal of Phycology*, 12(4), 421–430. <https://doi.org/10.1111/j.1529-8817.1976.tb02866.x>
- Prokopenko, M. G., Pauluis, O. M., Granger, J., & Yeung, L. Y. (2011). Exact evaluation of gross photosynthetic production from the oxygen triple-isotope composition of O_2 : Implications for the net-to-gross primary production ratios. *Geophysical Research Letters*, 38, 1–5. <https://doi.org/10.1029/2011GL047652>
- Redfield, A. C. (1963). The influence of organisms on the composition of sea-water. *The sea*, 2, 26–77.
- Siegel, D. A., Doney, S. C., & Yoder, J. A. (2002). The North Atlantic spring phytoplankton bloom and Sverdrup's critical depth hypothesis. *Science*, 296(5568), 730–733. <https://doi.org/10.1126/science.1069174>
- Sosik, H. M., & Olson, R. J. (2007). Automated taxonomic classification of phytoplankton sampled with imaging-in-flow cytometry. *Limnology and Oceanography*, 5(6), 204–216. <https://doi.org/10.4319/lom.2007.5.204>
- Sosik, H. M., Peacock, E., & Santos, M. (2020). *Abundance and biovolume of taxonomically-resolved phytoplankton and microzooplankton imaged continuously underway with an Imaging FlowCytobot along the NES-LTER Transect in winter 2018 ver 1*. Retrieved from <https://doi.org/10.6073/pasta/74775c4af51c237f2a20e4a8c011bc53>
- Stanley, R. H. R., Kirkpatrick, J. B., Cassar, N., Barnett, B. A., & Bender, M. L. (2010). Net community production and gross primary production rates in the western equatorial Pacific. *Global Biogeochemical Cycles*, 24(4), 1–17. <https://doi.org/10.1029/2009GB003651>
- Zimmermann, J., Jahn, R., & Gemeinholzer, B. (2011). Barcoding diatoms: Evaluation of the V4 subregion on the 18S rRNA gene, including new primers and protocols. *Organisms Diversity & Evolution*, 11(3), 173–192. <https://doi.org/10.1007/s13127-011-0050-6>

Geophysical Research Letters

Supporting Information for

Diatom Hotspots Driven by Western Boundary Current Instability

Hilde Oliver¹, Weifeng G. Zhang¹, Walker O. Smith, Jr.,^{2,3} Philip Alatalo¹, P. Dreux Chappell⁴, Andrew J. Hirzel¹, Corday R. Selden⁴, Heidi M. Sosik¹, Rachel H. R. Stanley⁵, Yifan Zhu⁴, and Dennis J. McGillicuddy, Jr.¹

¹Woods Hole Oceanographic Institution, Woods Hole, MA, USA

²Virginia Institute of Marine Science, College of William & Mary, Gloucester Point, VA, USA

³School of Oceanography, Shanghai Jiao Tong University, Shanghai, People's Republic of China

⁴Department of Ocean and Earth Sciences, Old Dominion University, Norfolk, VA USA

⁵Department of Chemistry, Wellesley College, Wellesley, MA, USA

Contents of this file

Text S1 to S12
Figures S1 to S10
Tables S1 to S3

Additional Supporting Information (Files uploaded separately)

Caption for Dataset S1

Introduction

The Supporting Information text primarily details the collection and processing of the data presented in the main text, in addition to describing the methodology used for the bio-optical model and the 1D physical-biological model. The included Figures and Tables provide additional visualizations to complement the Main Text, as well as to support the Supporting Information text.

Supplementary Information Text

Text S1. CTD profiling and bottle sampling

The CTD rosette was equipped with a SeaBird 911 CTD system, a WetLabs ECO-AFL/FL fluorometer, and a photosynthetically active radiation (PAR) sensor. Surface PAR levels were also measured. PAR, temperature, salinity, and fluorescence were measured on all CTD casts.

Twenty-four 10 L Niskin bottles fitted with Teflon-coated external closures were used for water column sampling. At each station, samples were typically collected at 12 discrete depths for assessment of nutrient concentrations. These samples were syringe-filtered and stored at -20°C until analysis at the WHOI Nutrient Analytical Facility. Nitrate and silicate were measured using standard AutoAnalyzer techniques. To measure ammonium concentrations, site water was cartridge-filtered (0.1 µm, Pall Co.) directly from Niskin bottles using a peristaltic pump. Filtrate was collected in Falcon™ tubes that were pre-treated with orthophthaldialdehyde (OPA) and measured on-board via the OPA method (Holmes et al., 1999) with a detection limit of 10 nM.

To measure particulate organic carbon and nitrogen, water was collected from the Niskin bottles and filtered through combusted 0.7 µm glass fiber filters (Whatman GF/F), rinsed with a weak acid (0.01 N HCl in seawater) to remove carbonates, then dried in combusted glass vials at 60 °C. Diatom biomass was assessed by sampling for biogenic silica. Samples were filtered through 0.6 µm polycarbonate filters, dried at 60°C in plastic Petri dishes, and dissolved in strong acid.

Fluorescence was converted into chlorophyll *a* concentrations using a regression between fluorescence values and extracted chlorophyll *a* measurements from Niskin bottles. CTD fluorescence (FL) was converted to chlorophyll *a* concentration with the following regression:

$$\mathbf{Chl\ a = 0.50FL + 0.13} \quad \mathbf{(1)}$$

Which has $R^2 = 0.88$.

Text S2. Video Plankton Recorder Surveys

To assess the large microplankton and small mesoplankton community alongside fine-scale measurements of temperature, salinity, and fluorescence, a Video Plankton Recorder II (VPR, from SeaScan Inc.) was towed behind the ship. The VPR consists of a towed body, containing a Seabird Electronics Inc. CTD (SBE 49 FastCat), oxygen sensor (SBE 43), fluorometer (ECO FLNTU-4050), ECO Triplet (ECO BBFL2-123), PAR (photosynthetically active radiation; Biospherical Instruments Inc. QCP-200L), and a synchronized video camera and xenon strobe (Davis et al., 2005). The VPR was towed at 10 knots (5.1 m s⁻¹), undulating between depths as shallow as 5m and as deep as 120m approximately every 6 minutes. This provided a minimum horizontal resolution of 1.8 km throughout the tow. For this study, we show data from VPR surveys 3, 7, and 8, which consisted of 234, 126, and 110 complete transits from the surface to 120 m.

Concentrations of chlorophyll *a* were determined from fluorescence by regressing chlorophyll values from the CTD casts immediately following the three VPR transects,

using the fluorescence (FL) from the nearest VPR oscillation to the CTD profile. The regression used was

$$Chl\ a = 0.59FL + 0.13 \quad (2)$$

which has $R^2 = 0.81$.

Text S3. REMUS 600 hotspot survey

On July 12-13, the autonomous underwater vehicle (AUV) REMUS 600 was deployed to survey the hotspots (Fig. S9). The AUV was equipped with a CTD, a WET Labs - ECO Triplet sensor, and an optical nitrate sensor (Submersible Ultraviolet Nitrate Analyzer-SUNA). REMUS chlorophyll *a* and nitrate concentrations were determined from AUV measurements by regressing chlorophyll and nitrate values from the CTD casts and bottle nutrient measurements immediately preceding the REMUS survey, applying values from the nearest REMUS oscillation to the CTD profile. For chlorophyll, we use the regression

$$Chl\ a = 0.70FL + 0.30 \quad (3)$$

which has $R^2 = 0.55$. For nitrate, we use the regression

$$NO_3 = 0.75[SUNA\ NO_3] - 2.87 \quad (4)$$

which has $R^2 = 0.88$.

Text S4. Imaging FlowCytobot

The Imaging FlowCytobot (IFCB) records high-resolution ($\sim 1\ \mu\text{m}$) images of a wide variety of phytoplankton taxa, from those $< 10\ \mu\text{m}$ to those hundreds of microns long (Sosik & Olson, 2007). The IFCB is equipped with a red diode laser; the laser light is scattered as particles pass through. Frame capture from a CCD camera was triggered by both fluorescence and scattering. The high-quality images allow the identification of many taxa to the genus level. IFCB images were recorded from Niskin bottles taken both within and outside the biomass peaks at hotspot stations. Images were processed using the methods described in (Sosik et al., 2020), with biovolume calculated with the method described in Moberg & Sosik, 2012. Results in Fig. 3 are based on cell, chain, and colony biovolumes summed over the designated taxonomic groupings. Due to the lower size range detection limit for IFCB, only targets $> 5\ \mu\text{m}$ (in terms of either equivalent spherical diameter or maximum Feret diameter) were included in the biovolume sums. For species and genus level information about diatom contributions (Fig. 3b, taxa that contributed 8% or more to total diatom biovolume at any depth are shown explicitly; taxa consistently below that threshold are aggregated as "other diatoms").

Text S5. VPR automated classification of diatom rods

Diatom distributions were measured in situ using the VPR. Plankton video was collected at 30 Hz. Individual 1380 x 1034 pixel video frames ($\sim 20\ \text{mm} \times 15\ \text{mm} \times 23\ \text{mm}$

volume imaged) were passed through object-identification software to identify “regions of interest” (ROIs), which were then saved to disk with a time-stamp naming convention. ROIs were automatically classified using a convolutional neural network (CNN) specifically designed for plankton (González et al., 2019). The CNN was trained using approximately 1000 manually annotated ROIs for 29 categories (Table S1). The training dataset was composed of ROIs from two cruises, the March 2018 *R/V Neil Armstrong* cruise AR29 and the July 2019 *R/V Thomas G. Thompson* cruise TN368. Most categories were trained with ROIs solely from TN368, but three (echinoderm larvae, bloom conditions, and spherical colonial plankton) were from AR29. Bloom conditions were defined as ROIs that contained spherical colonial plankton (*Phaeocystis pouchetti* in the case of AR29), diatom chains, and marine snow. Diatom hotspot conditions within TN368 were composed of *Thalassiosira diporocyclus*, diatom chains, and marine snow. The globular morphology of *T. diporocyclus* was similar enough to *P. pouchetti* that the CNN associated the diatom hotspot observed in TN368 with the bloom condition category, enabling the use of the bloom condition category as a proxy for diatom hotspot conditions.

CNN accuracy by taxon was determined by F1 score ($F1 = 2 * (\text{precision} * \text{recall}) / (\text{precision} + \text{recall})$). Precision (true positives / (true positives + false positives)) and recall (true positives / (true positives + false negatives)) were determined by withholding 20% of the original training set ROIs for each taxon and running the CNN on the withheld ROIs. The overall CNN F1 score was 86.64%.

To quantify the accuracy of the diatom distributions, the first 100 ROIs from each hour classified as diatom chains were checked for false positives. This yielded a mean false positive rate of approximately 17.4%. False negative rates were computed by counting the number of false negatives for the first 250 ROIs of each hour within VPR Tow 2 in the following categories: bloom conditions (51.8%), bubbles (0.6%), marine snow (2.3%), out-of-focus (2.4%), and unknown (6.8%). These categories were chosen because they were the most abundant within the tow, each containing more than 10,000 ROIs. Out-of-focus was the most abundant category, containing approximately four times as many classified ROIs (294,809) as that of diatom chains (61,153). The other categories contained approximately the same number of ROIs as that of diatom chains (bubbles = 55,505; marine snow = 45,417; unknown = 89,389), except bloom conditions, which contained 13,049 ROIs.

To account for the impact of false negatives on the diatom distributions, the counts were augmented with an estimate computed by multiplying the rate of false negatives for each hour by the taxon concentrations within that hour (i.e., $\text{diatom}_{\text{xyz hour}} = \text{diatom}_{\text{original xyz hour}} + (\text{non-diatom taxon}_{\text{xyz hour}} * \text{false negative rate}_{\text{hour}})$). The inclusion of diatom chain false negatives from other categories increases the diatom chain absolute abundance by approximately a factor of three, without changing their geographical distribution (Fig. S4).

Precise quantification of diatom concentrations is further challenged by the fact that there were highly variable numbers of diatom chains per ROI in the cores of the hotspots, in addition to colonial forms of *T. diporocyclus* and marine snow. The density of material in the bloom conditions category was such that in-focus objects were often

occluded by out-of-focus objects, making the enumeration of diatoms within individual ROIs difficult, time-consuming, and subjective. As such, ascertaining the peak concentration of diatoms within the hotspots is impractical.

We therefore decided to present our results in terms of relative diatom concentration using the “diatoms” category, which consists primarily of single in-focus diatom chains. The resulting maps are a reliable proxy for the overall diatom distribution, recognizing of course that the peak concentrations in the inner cores of the diatom hotspots are underestimated.

Text S6. DNA Sequencing and Analysis

Water samples were collected in acid-washed (10% HCl) 4 L amber polypropylene bottles from Niskin bottles and gently filtered (1 to 5 L) onto 0.22 μm polyethersulfone membrane filters (Sterivex™, MilliporeSigma, USA) using a peristaltic pump. Invitrogen RNA_{later} stabilizing solution (ThermoFisher Scientific, USA) was applied to filters following manufacturer specifications. Following the overnight preservation at 4°C, samples were stored in liquid nitrogen (during the cruise) or at -80°C (in the lab) until processing. Before nucleic acid extractions, samples were thawed and the stabilizing solution was vacated. The filter was then removed from the Sterivex™ frame and submerged in RLTPlus buffer (1% β -mercaptoethanol by volume; Qiagen, Germany). Filters were bead-beaten for 2 min using 0.1 and 0.5 μm silica beads to facilitate cell break-down. Finally, the lysate was homogenized using a QIAshredder Spin column (Qiagen, Germany). DNA and RNA were then co-extracted with the AllPrep DNA/RNA Mini Kit (Qiagen, Germany).

The V4 region of 18S rDNA was amplified in triplicate using a polymerase chain reaction (PCR) method (Chappell et al., 2019). The primers employed were designed specifically for diatom DNA barcoding (Zimmermann et al., 2011) modified for two-step amplicon sequencing with Illumina (USA) technology. Replicate PCR products were pooled, verified via gel electrophoresis, and purified (GeneJet PCR Purification Kit; ThermoFisher Scientific, USA). The Nextera DNA Library Preparation Kit (Illumina, USA) was used to prepare the DNA library. In brief, purified PCR products were diluted to < 55 ng DNA μl^{-1} and indexed in a 50 μl reaction following the manufacturer’s protocol. Phusion High-Fidelity PCR Master Mix with HF Buffer (ThermoFisher Scientific, USA) was used in this reaction. Second-round PCR products were cleaned using Ampure XP paramagnetic beads following manufacturer’s protocol (Beckman Coulter, USA), quantified fluorometrically (Invitrogen Qubit 2.0, ThermoFisher Scientific, USA), and diluted to 4 nM. The quality of a subset of samples was evaluated with a Fragment Analyzer System (Agilent Technologies Inc., USA). High-quality samples were then pooled. To improve the quality of sequencing reads, the multiplexed amplicon library was combined 85:15 with PhiX Control v3 Library (4nM, Illumina, USA). The amplicon library was sequenced on an Illumina MiSeq platform using the Illumina v3 2 \times 300 cycle kit.

Diatom 18S rDNA amplicon sequences were de-multiplexed and analyzed using the DADA2 pipeline (version 1.16.0, Callahan et al., 2016). At the start of the pipeline, primers were removed using cutadapt (version 2.10, Martin, 2011). The following

parameters were used to filter reads using the DADA2 filterAndTrim command: maxN = 0, truncLen = c(230,190), maxEE = c(2,2), truncQ = 2, minLen = 50, rm.phix = TRUE. After the DADA2 algorithm generated initial amplicon sequence variants (ASVs), ASVs shorter than 395 or longer than 410 were filtered out. Additionally, chimeric ASVs were filtered out using the removeBimeraDenovo command with the following parameters: method = "consensus", minFoldParentOverAbundance = 8.

The taxonomic assignment of the ASVs followed the protocol of Chappell et al. 2019. The ASV FASTA file was used as an input for a nucleotide BLAST (Altschul et al., 1990) against an in-house database that combined Stramenopile 18S sequences from NCBI (downloaded as of 23 June 2020) and the SILVA eukaryote 18S database. ASVs that did not have a diatom as a top hit were not included in subsequent analyses. ASVs were classified to the species level if they had a >99% identity to a diatom sequence. ASVs were classified as species-like (akin to the cf. designation in morphology) if they had 98-99% identity to a diatom sequence. ASVs with a <98 % identity to a diatom sequence were only classified to the genus level. PRIMER v.7 (Clarke & Gorley, 2018) was used to log transform ASV counts and generate a Bray-Curtis similarity matrix (Bray & Curtis, 1957) that was visualized in a cluster dendrogram generated using the group average clustering mode.

Text S7. Incubation-based primary productivity

Water samples were taken from Niskin bottles at known isolumes, then placed in sterile 285 mL Qorpak bottles, then ~20 μCi $\text{NaH}^{14}\text{CO}_3$ was added. An on-deck incubator holding the bottles had surface seawater flowing through it, with irradiance attenuated by neutral density filters to the light levels at the isolumes sampled. Blue filters were used for isolumes below 30% E_0 . After 24 h, samples were filtered through GFF filters and placed in 7 mL scintillation vials. Size fractionations were conducted at all stations using 20 μm Poretics filters on subsamples from each bottle. 100 μL 1N HCl was added to volatilize absorbed inorganic ^{14}C . Ecolume (5 mL) was then added to each vial, and all vials were counted after 24 h on a liquid scintillation counter. Total activity was measured by counting 100 μL of non-acidified sample in β -phenethylamine.

Text S8. Bio-optical model

Productivity was estimated using a bio-optical model (Fig. S6c, d, g). The model was based on the formulation of Behrenfeld & Falkowski (1997a, 1997b), where depth-resolved productivity is a function of temperature, irradiance (PAR), and chlorophyll concentrations (Eq. 5).

$$PP = C_z \times P_{opt}^B \times f(E_0) \quad (5)$$

where **PP** is primary productivity, **C_z** chlorophyll concentration, **P_{opt}^B** the maximum photosynthetic rate within the water column, and **f(E₀)** an irradiance function within the water column, where **E₀** is surface PAR. A photosynthesis-irradiance response (Jassby & Platt, 1976) was used:

$$P_z^B = P_{opt}^B \times \tanh \left[E_z / E_k \right] \quad (6)$$

At station SLP in the slope sea cyclonic feature (CTD Cast 100), the chlorophyll-normalized carbon fixation rate of hotspot phytoplankton was highest at 15% of surface irradiance levels (45 m depth, Fig S6a), so $E_k = 0.15 \times$ (surface PAR) where $PAR < 100 \mu\text{mol photons m}^{-2} \text{s}^{-1}$, and $E_k = 0.25 \times$ (surface PAR) when $PAR > 100 \mu\text{mol photons m}^{-2} \text{s}^{-1}$.

P_{opt}^B was derived by the 7th order polynomial that was based on 1,698 radioisotope measurements made throughout the ocean (Behrenfeld & Falkowski, 1997b). A photoinhibition multiplier based on the same data set was used to reduce productivity due to photoinhibition when irradiance was $> 3 \text{ mol photons m}^{-2} \text{d}^{-1}$ (Eq. 7) (Behrenfeld & Falkowski, 1997b):

$$P_{inh} = -0.0204E_0^2 + 2.515E_0 - 6.675 \quad (7)$$

E_z values were derived from the relationship described by Platt & Jassby, (1976).

To generate irradiance attenuation profiles, the relationship between chlorophyll and attenuation in daytime casts (Morel, 1974) was used to correct for an offset that was observed. We believe this offset was due to dissolved organic carbon that originated from the continental shelf. To compare all stations, we used a constant surface irradiance, which was equal to that of a clear sky irradiance value. Productivity was estimated from the above equations at 1-m intervals from the surface to the 1% isolume, defined as the absolute compensation irradiance $1.3 \mu\text{mol photons m}^{-2} \text{d}^{-1}$ estimated for the North Atlantic (Siegel et al., 2002). Note that the bio-optical model accounts for declining carbon fixed per unit chlorophyll with declining light (Fig. S6e, jumps in the profiles 10-30 m above the absolute compensation irradiance indicate the transition from $E_k = 0.25 \times$ surface PAR to $E_k = 0.15 \times$ surface PAR). At the surface, the carbon fixed per unit chlorophyll is 7 ± 3 times greater than at the hotspots of maximum productivity (Fig. S6e). Measured ratios of POC to chlorophyll vary widely at the hotspot productivity maximum layers, suggesting potentially high concentrations of marine snow (Fig. S6f), and therefore were not applicable for constraining C:Chl ratios within hotspot algal biomass.

Model performance was also assessed for non-hotspots casts conducted for TN368. The model was run for all primary productivity casts (Fig. S6g, h), and then compared against the incubation productivity (Fig. S6h, i). The model was likely to either over- or underestimate the incubation productivity at most stations, excepting inner shelf stations 41, 43, and 80 (shown by magenta circles on map in Fig. S7), where modeled productivity was much lower than measured (Fig. S6i). Chlorophyll was higher than other shelf stations in the top 20-30 m at these stations (Fig. S6g), but the measured productivity is enhanced as shallow as the sea surface. The model photoinhibition term thus may not be applicable when modeling these stations.

The incubation integrated productivity suggests higher productivity on the shelf and lower productivity within the hotspots, excepting cast 84 where the chlorophyll

maximum productivity was measured (Fig. S7a). The modeled productivity is similar between the hotspots and the shelf, however (Fig S7b), and predicts higher integrated productivity at all hotspot stations relative to the incubation integrated productivity (Fig S7c), despite closely reproducing profiles of measured productivity at the hotspot casts (Fig S6d). While the model typically underestimates productivity for non-hotspot casts, with the inter-quartile range of model-incubation productivity differences for non-hotspot casts being less than 0, the model projects higher productivity for all hotspot casts (Fig. S7e).

To assess model sensitivity and uncertainty, we conducted an error perturbation analysis on the bio-optical model, modifying key parameters over their uncertainties: upper water column light attenuation coefficient k_d (± 0.01 , unitless), measured chlorophyll a concentration ($\pm 5\%$), and absolute compensation irradiance ($\pm 0.3 \mu\text{mol photons m}^{-2} \text{d}^{-1}$). We reran the bio-optical model for each parameter mean, minimum, maximum combination, for a total of 27 runs, as done in the error perturbation analysis in Friedrichs et al. (2009). The maximum perturbation to integrated productivity while varying each parameter one at a time, and all parameters simultaneously are reported in Table S2. Error sums in quadrature are also reported in Table S2. We use the maximum perturbation when varying all parameters simultaneously when reporting the modeled vs. measured difference in integrated productivity.

Text S9. Gross Primary Production estimate from triple oxygen isotopes

Triple oxygen isotopes of dissolved oxygen quantify the fraction of oxygen-derived from photosynthesis rather than from atmospheric oxygen. Profiles of triple oxygen isotopes (Fig. S8) show that photosynthetic oxygen was enhanced in the hotspots compared to samples collected at similar depths but non-hotspot locations on the cruise. Typically, triple oxygen isotopes are used in surface waters to estimate mixed layer gross primary production (GPP). In this case, however, we are interested in GPP below the mixed layer – at a depth of ~ 50 m in the diatom hotspot. We also do not have a time-series (as in Juranek & Quay, 2013) and thus do not know the amount of time it takes for the triple oxygen isotopic signature to change. As a result, we cannot exactly quantify GPP. However, we can estimate GPP by assuming the deep water (100 m depth) is the source water for the diatom hotspot – or at least has analogous triple oxygen isotopic composition - and that the transit time was about 2 weeks (Fig. 1). The current best practice is to calculate GPP from $\delta^{17}\text{O}$ and $\delta^{18}\text{O}$. However, in this case, since we are calculating GPP below the surface and do not have a regular time series, the equations in Prokopenko et al. (2011) and Kaiser (2011) are not suitable. We thus perform a rough calculation based on the $^{17}\Delta$ where $^{17}\Delta$ is defined as

$$^{17}\Delta = 10^6 \times \left(\left(\frac{\delta^{17}\text{O}}{1000} + 1 \right) - \lambda \left(\frac{\delta^{18}\text{O}}{1000} + 1 \right) \right)$$

(8)

where $\delta^{17}\text{O} = (^{17}\text{O}_{\text{meas}}/^{17}\text{O}_{\text{air}} - 1) \times 1000$, and $\lambda = 0.5179$ (Luz & Barkan, 2005), corresponding to the fractionation associated with respiration (Fig. S8). As described by Hendricks et al. (2004) the ratio R of photosynthetic oxygen to atmospheric oxygen in a water sample is

$$R = \frac{{}^{17}\Delta_{eq} - {}^{17}\Delta_{meas}}{{}^{17}\Delta_{meas} - {}^{17}\Delta_{eq} - {}^{17}\Delta_P} \quad (9)$$

where ${}^{17}\Delta_{eq}$ is the ${}^{17}\Delta$ signature of water equilibrated with atmospheric oxygen = 8 per meg (Stanley et al., 2010), ${}^{17}\Delta_{meas}$ is the ${}^{17}\Delta$ signature measured in a particular water sample, and ${}^{17}\Delta_P$ is the ${}^{17}\Delta$ signature of oxygen produced completely from photosynthesis = 249 per meg (Luz & Barkan, 2000). Therefore, the fraction of photosynthetic oxygen in the water, f_P , is given by:

$$f_P = \frac{R}{R + 1} \quad (10)$$

assuming the only sources of oxygen are photosynthetic or atmospheric.

By combining the fraction of photosynthetic oxygen measured at the diatom hotspot depth (47 m at Station 71) and at the deep source water depth (denoted $f_{P,hs}$ and $f_{P,d}$ respectively) with the oxygen concentration at the hotspot and deep depths ($[\text{O}_2]_{hs}$ and $[\text{O}_2]_d$ respectively), it is possible to calculate the total amount of photosynthetic oxygen, $[\text{O}_2]_{photo}$, added to the water during the transit time when the 100 m water (or source water with analogous oxygen characteristics) was transported to the diatom hotspot:

$$[\text{O}_2]_{photo} = \frac{(f_{P,hs}[\text{O}_2]_{hs} - f_{P,d}[\text{O}_2]_d - \alpha([\text{O}_2]_{hs} - [\text{O}_2]_d))}{(1 - \alpha)} \quad (11)$$

where α is the fraction of oxygen that has been respired that was photosynthetic in origin. If all the respiration happened at the beginning of the transit, then α would equal $f_{P,d}$. If all the respiration happened at the end of the transit, α would equal $f_{P,hs}$. We assume that α is an average of those two possibilities but we also calculate $[\text{O}_2]_{photo}$ using both extremes.

Finally, the rate of GPP, in O_2 units, is given by:

$$GPP = \frac{[\text{O}_2]_{photo}}{\Delta t} \quad (12)$$

where Δt is the assumed time required for transporting the source water to the hotspot.

The triple oxygen isotopic signature, ${}^{17}\Delta_{meas}$, was measured on an isotope ratio mass spectrometer after the samples had been purified to remove all gases other than O_2 and Ar from the samples (Stanley et al., 2010). Δt is estimated to be 14 days (Fig. 1). Oxygen concentration was measured by an SBE O_2 sensor on the CTD. The O_2 sensor has been calibrated in the factory within six months. It was not calibrated on the cruise but since

the difference in hotspot and deep O₂ concentrations is used in this calculation, and this calculation is only a rough estimate due to large unknown in other parameters, a lack of onboard calibration should not lead to significant errors. The measurement uncertainty of ¹⁷Δ based on equilibrated water samples measured during the same period is 5 per meg. The largest source of uncertainty in the calculation comes from the estimates of α and Δt.

The best estimate of GPP, as calculated from comparing the 47 m diatom hotspot sample on cast 71 to the 100 m estimated source water sample from the same cast is 5.7 mmol O₂ m⁻³ d⁻¹, which equals 4.0 mmol C m⁻³ d⁻¹ using a photosynthetic quotient of 1.4. With α equal to the two extremes of f_{P,d} or f_{P,hs}, then the GPP rate ranges from 4.5 mmol O₂ m⁻³ d⁻¹ = 3.2 mmol C m⁻³ d⁻¹ to 7.5 mmol O₂ m⁻³ d⁻¹ = 5.3 mmol C m⁻³ d⁻¹. Given GPP is expected to be roughly a factor of 2.6 larger than NPP, this estimate agrees well with the completely independent estimate of NPP based on the ¹⁴C incubations and bio-optical model.

Text S10. Euphotic depth calculation for Fig. 4

For Fig. 4, the euphotic depth is calculated as the depth of 1% of surface irradiance. Irradiance (*I*) at each depth of the VPR and REMUS 600 data is determined by:

$$\frac{\partial I}{\partial z} = -k_d I \quad (13)$$

where *k_d* is the light attenuation coefficient, and

$$k_d = k_z + k_p [\text{Chl } a] \quad (14)$$

where *k_z* is light attenuation of clear seawater (*k_z* = 0.04 m⁻¹), and *k_p* is the light attenuation from phytoplankton biomass (*k_p* = 0.13 ± 0.04 (μg Chl a L⁻¹)⁻¹ m⁻¹). We derived *k_p* using CTD profiles of photosynthetically active radiation (PAR) from daytime casts from the slope and the shelf, determining for each cast the value of *k_p* that results in the closest 1% light depth to that determined by the ratio of PAR on the rosette to surface PAR sensor values. The two 1% isolumes shown in Fig. 4 contain the 1% depth when applying the *k_p* range of the mean ± 1 standard deviation (*k_p* = 0.09 – 0.16 (μg Chl a L⁻¹)⁻¹ m⁻¹).

Text S11. One-dimensional model

We selected the model initial temperature and salinity profiles using the 1^o summer objectively analyzed climatological means from the National Centers for Environmental Information (NCEI) Northwest Atlantic Regional Ocean Climatology (Seidov, 2016), and nitrate profiles using the 2018 NCEI World Ocean Atlas (Garcia et al., 2019). We initialize the 1D model with the climatological profile south of the MAB most closely satisfying the definition of the GS northern edge (temperature at 200 m = 15°C (Joyce et al., 2000); location shown by white star in Fig. 1A; profiles shown in gray in Fig. 5A).

To simulate macronutrient drawdown, we couple a dissolved inorganic nitrogen (DIN), silicic acid (dSi), and light-limited nitrogen-phytoplankton-zooplankton-detritus (NPZD) biogeochemical model to the physical model (adapted from the Powell NPZD model (Powell et al., 2006); see Text S12 for model equations and parameters). We derive the slope water light-attenuation coefficient using profiles of photosynthetically active radiation (PAR) from daytime casts during TN368. We assume a POC:Chl ratio of 50 and a C:N ratio of 106:16 (Redfield, 1963).

We ran the model for one month (1 Jul – 31 Jul 2019), with a time step of 300 s, and a constant vertical resolution of 10 cm. We assume that the GS upwelling and phytoplankton bloom would take no longer than one month to develop because the large features characterizing the MAB slope region generally take 1-3 weeks to evolve, such as the intrusion of the meander onto the shelfbreak and the development of the WCR streamer (Fig. 1).

The upward vertical velocity was held constant over the entire model period and is applied to the NCEI GS endmembers. To prevent the upward velocities resulting in shallower mixed layers, we impose a constant mixed layer depth of 17 m, taken as the mean of all TN368 CTD mixed layer depths from the slope sea (defined where salinity at 10 m is > 34.6 , with the mixed layer depth defined as the depth where the potential density change from the surface value reaches $\Delta\rho = 0.04 \frac{kg}{m^3}$). To account for fluxes from below, we apply a gradient boundary condition at the base of the model for temperature, salinity, nitrate, and silicate. We use a vertically uniform diffusivity $K_z = 10^{-5} m^2 s^{-1}$.

Model surface forcing was downloaded from National Centers for Environmental Prediction – National Center for Atmospheric Research (NCEP/NCAR) July 2019 mean reanalysis fields of surface air temperature, latent heat flux, net longwave radiation, net shortwave radiation, precipitation rate, surface air pressure, and wind stress from 72°W – 69°W and 37°N – 39°N (Kalnay et al., 1996).

We tested the model with a range of maximum vertical velocities based on those likely to occur at the edge of a WCR (Zhang & Partida, 2018). A vertical velocity of $10^{-4} m s^{-1}$ at 150 m results in the best matchups between temperature, salinity, nitrate, and chlorophyll between the model and observations at station SLP. We note that because the biogeochemical parameters and initial biomass concentrations can be tuned to result in smaller model-data differences with a given vertical velocity, our chosen upwelling rate is merely one out of many possible values.

Text S12. Biogeochemical model details and equations.

State variables in the biogeochemical model nitrogen and silicon budgets are phytoplankton biomass (**P**), zooplankton biomass (**Z**), small detritus (**SD**), and large detritus (**LD**). Fluxes include nutrient uptake (**U**), grazing (**G**), excretion, egestion, mortality, aggregation, and remineralization. Phytoplankton growth (= net nutrient uptake, **U**) is the product of the maximum growth rate, light availability, and nutrient availability. Nutrient availability is the availability of the scarcer nutrient (Liebig's law of the minimum). We also incorporate elements of the model developed by Fennel et al.,

(2006) by using a Holling-type formulation for grazing, and the second-order aggregation of phytoplankton and small detritus into large detritus. Our model includes zooplankton assimilation efficiency (β_N), excretion (γ_n), mortality (ζ_d), remineralization (δ), and aggregation (τ) (Table S3).

The governing nitrogen model state equations are as follows (terms in units of μM or $\mu\text{M d}^{-1}$, with parameters as defined in Table S3):

$$\underbrace{\frac{\partial \text{DIN}}{\partial t}}_{\text{dissolved inorganic N}} = \underbrace{-UP_N}_{\text{uptake by phytoplankton}} + \underbrace{\gamma_n GZ_N}_{\text{zooplankton excretion}} + \underbrace{\delta \text{SD}_N + \delta \text{LD}_N}_{\text{remineralization}} \text{LD}_N \quad (15)$$

$$\underbrace{\frac{\partial P_N}{\partial t}}_{\text{phytoplankton}} = \underbrace{+UP_N}_{\text{uptake}} - \underbrace{GZ_N}_{\text{grazing}} - \underbrace{\sigma_{P1} P1_N}_{\text{mortality}} - \underbrace{\tau (\text{SD}_N + P_N) P_N}_{\text{aggregation}} - \underbrace{w_P \frac{\partial P_N}{\partial z}}_{\text{sinking}} \quad (16)$$

$$\underbrace{\frac{\partial Z_N}{\partial t}}_{\text{zooplankton}} = \underbrace{\beta GZ_N}_{\text{grazing}} - \underbrace{\gamma_n GZ_N}_{\text{excretion}} - \underbrace{\zeta_d Z_N}_{\text{mortality}} \quad (17)$$

$$\underbrace{\frac{\partial \text{SD}_N}{\partial t}}_{\text{small detritus}} = \underbrace{+\sigma_P P_N}_{\text{phytoplankton mortality}} - \underbrace{\tau (\text{SD}_N + P_N) \text{SD}_N}_{\text{aggregation}} - \underbrace{\delta \text{SD}_N}_{\text{remineralization}} - \underbrace{w_{SD} \frac{\partial \text{SD}_N}{\partial z}}_{\text{sinking}} \quad (18)$$

$$\underbrace{\frac{\partial \text{LD}_N}{\partial t}}_{\text{large detritus}} = \underbrace{+G(1-\beta) Z_N}_{\text{zooplankton egestion}} + \underbrace{\zeta_d Z_N}_{\text{zooplankton mortality}} + \underbrace{\tau (\text{SD}_N + P_N)^2}_{\text{aggregation}} - \underbrace{\delta \text{LD}_N}_{\text{remineralization}} - \underbrace{w_{LD} \frac{\partial \text{LD}_N}{\partial z}}_{\text{sinking}} \quad (19)$$

The governing silicon model state equations (with silica uptake converted from nitrogen uptake equations using an Si:N ratio, R) are as follows (terms in units of μM or $\mu\text{M d}^{-1}$, with parameter definitions in Table S3):

$$\underbrace{\frac{\partial d\text{Si}}{\partial t}}_{\text{silicate}} = \underbrace{-R \times UP_N}_{\text{uptake by phytoplankton}} + \underbrace{\delta \text{SD}_{Si} + \delta \text{LD}_{Si}}_{\text{remineralization}} \quad (20)$$

$$\underbrace{\frac{\partial P_{Si}}{\partial t}}_{\text{phytoplankton}} = \underbrace{+R \times UP_N}_{\text{uptake}} - \underbrace{P_{Si} \left(\frac{G Z_N}{P_N} \right)}_{\text{grazing}} - \underbrace{\sigma_P P_{Si}}_{\text{mortality}} - \underbrace{\tau (SD_N + P_N) P_{Si}}_{\text{aggregation}} - \underbrace{w_P \frac{\partial P_{Si}}{\partial z}}_{\text{sinking}} \quad (21)$$

$$\underbrace{\frac{\partial SD_{Si}}{\partial t}}_{\text{small detritus}} = \underbrace{+\sigma_P P_{Si}}_{\text{phytoplankton mortality}} - \underbrace{\tau (SD_N + P_N) SD_{Si}}_{\text{aggregation}} - \underbrace{\delta SD_{Si}}_{\text{reminerlization}} - \underbrace{w_{SD} \frac{\partial SD_{Si}}{\partial z}}_{\text{sinking}} \quad (22)$$

$$\underbrace{\frac{\partial LD_{Si}}{\partial t}}_{\text{large detritus}} = \underbrace{+P_{Si} \left(\frac{G Z_N}{P_N} \right)}_{\text{zooplankton egestion}} + \underbrace{\tau (SD_N + P_N) (SD_{Si} + P_{Si})}_{\text{aggregation}} - \underbrace{\delta LD_{Si}}_{\text{reminerlization}} - \underbrace{w_{LD} \frac{\partial LD_{Si}}{\partial z}}_{\text{sinking}} \quad (23)$$

The biogeochemical model uses the following functions:

Specific growth (uptake) rates for phytoplankton (U):

$$U = P_{max} \times \underbrace{\min \left(\frac{dSi}{k_{Si} + dSi}, \frac{DIN}{k_N + DIN} \right)}_{\text{limitation by most scarce nutrient}} \underbrace{\frac{\alpha I}{\sqrt{\alpha^2 I^2 + P_{max}^2}}}_{\text{light limitation}} \quad (24)$$

Photosynthetically active radiation (I , in $W m^{-2}$):

$$\frac{\partial I}{\partial z} = -k_d I \quad (25)$$

Light attenuation (k_d , in m^{-1}) from seawater ($k_z = 0.04$) and from phytoplankton biomass (k_p) (Fasham et al., 1990):

$$k_d = k_z + k_p P_N \quad (26)$$

Zooplankton grazing rates (Holling-type formulation, Fennel et al., 2006) on phytoplankton (G) in day^{-1} :

$$G = R_{max} \frac{P_N^2}{k_{phy} + P_N^2} \quad (27)$$

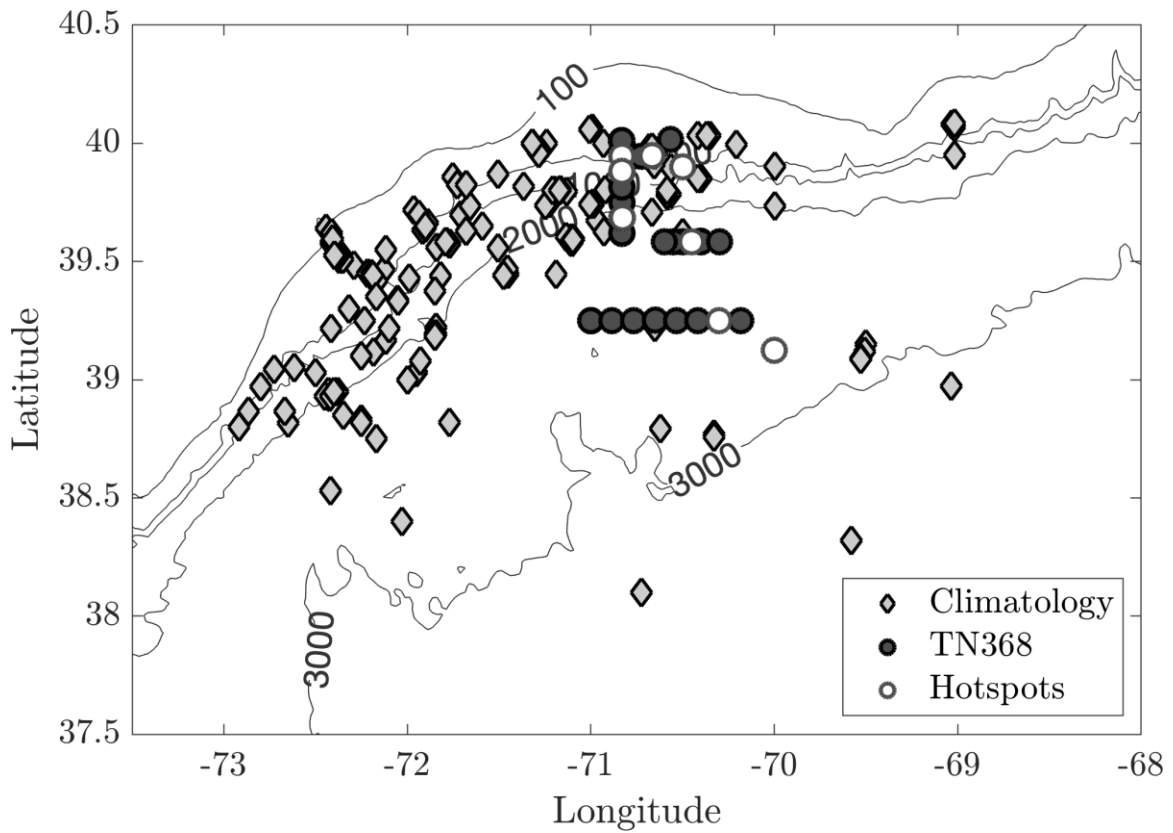


Fig. S1. Locations of June-September slope sea (bottom depth > 200 m) profiles from the MAB climatology (diamonds; Zhang et al., 2013) and TN368 (circles) used for the histogram in Figure 1D. Hotspot profiles are shown by white circles, and all other TN368 profiles are shown as dark gray circles.

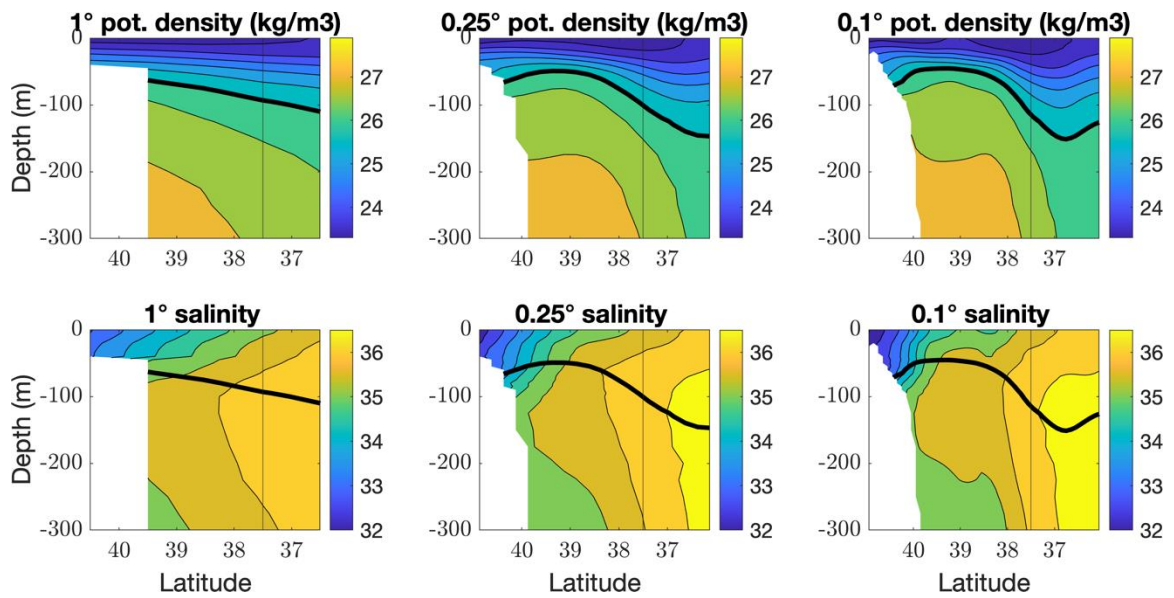


Fig. S2. North-south density and salinity cross-sections from NCEI NWA Summer Climatology at 70°W, for 1°, 0.25°, and 0.1° data product resolutions. Vertical lines at 37.5 show the location of the GS endmember profile, where $T(200\text{ m})$ is closest to 15°C in 1° climatology.

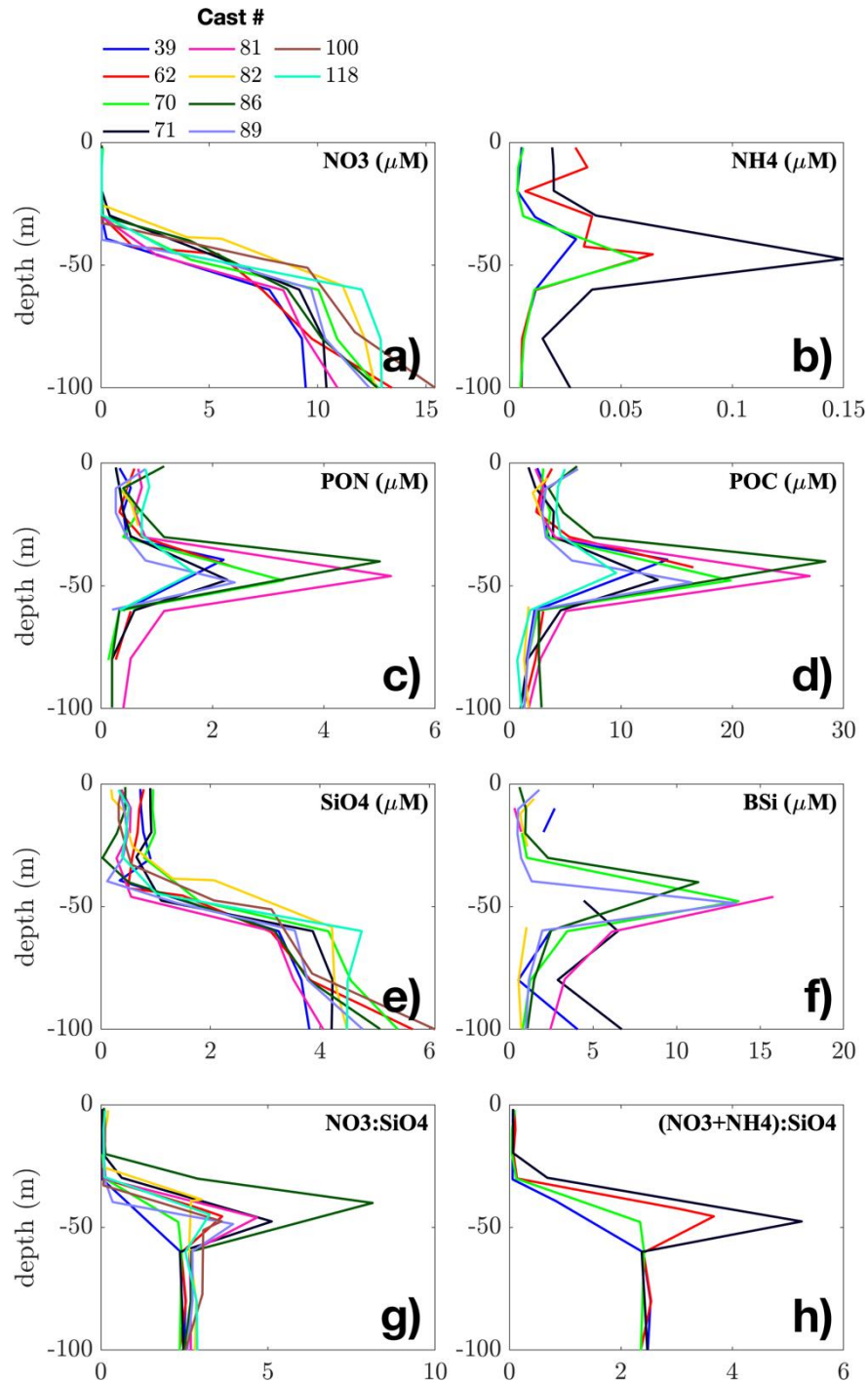


Fig. S3. Bottle file vertical profiles from hotspot CTD casts. Profiles include a) nitrate (NO₃), b) ammonium (NH₄), c) particulate organic nitrogen (PON), d) particulate organic carbon (POC), e) silicate (SiO₄), f) biogenic silica (BSi), g) nitrate to silicate ratios, and h) nitrate + ammonium to silicate ratios. Hotspot CTD casts are defined as casts where the chlorophyll maximum was between 35 and 50 m, the chlorophyll maximum was > 2.5 $\mu\text{g/L}$, and at the chlorophyll maximum salinity > 35.6.

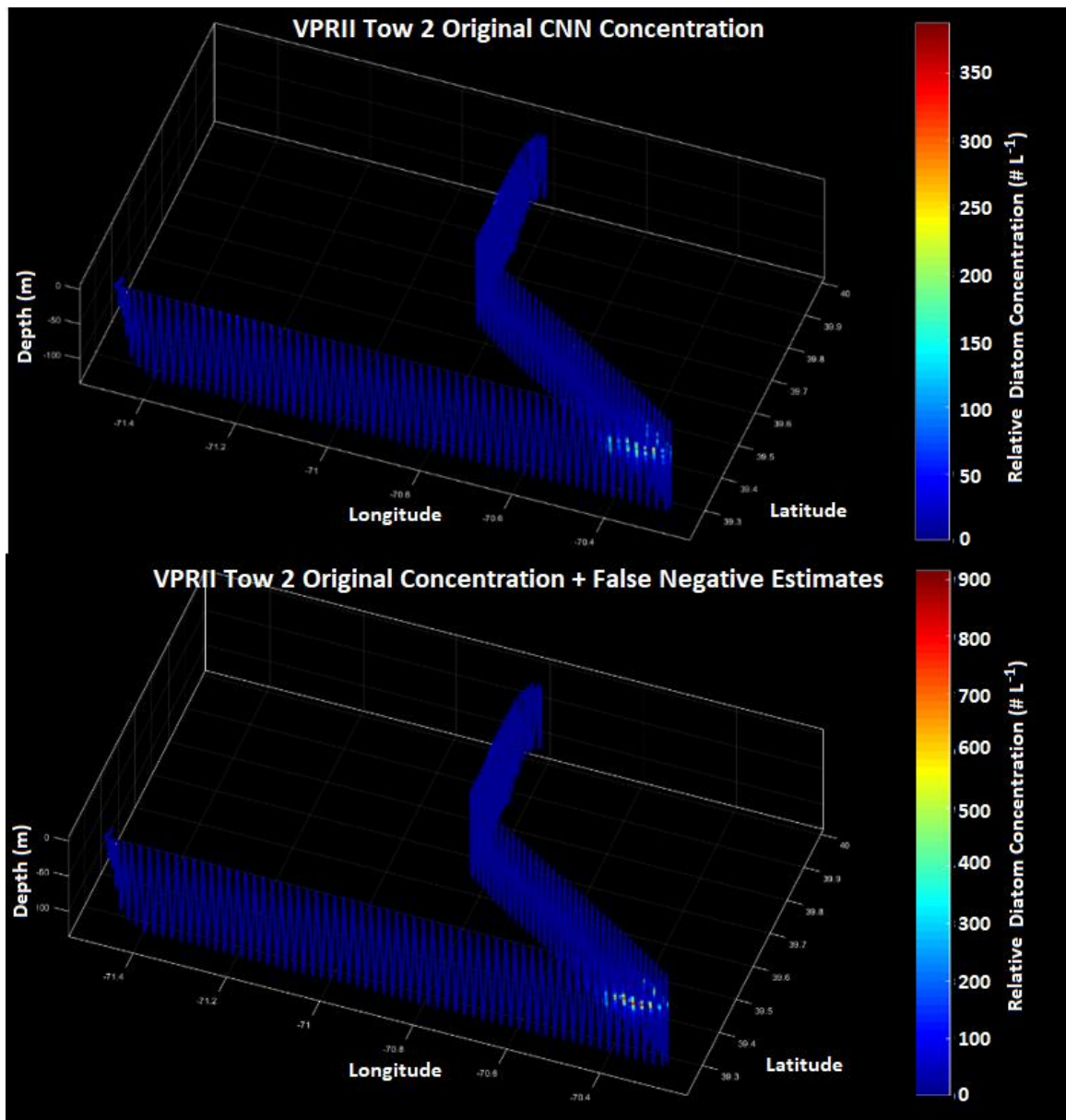


Fig. S4 Towed VPR diatom distributions. Top: original diatom distribution obtained from CNN classification without considering false positives and false negatives. Bottom: diatom distribution corrected for a theoretical maximum diatom concentration (original+false negatives) to determine an upper bound on the diatom hotspot concentration.

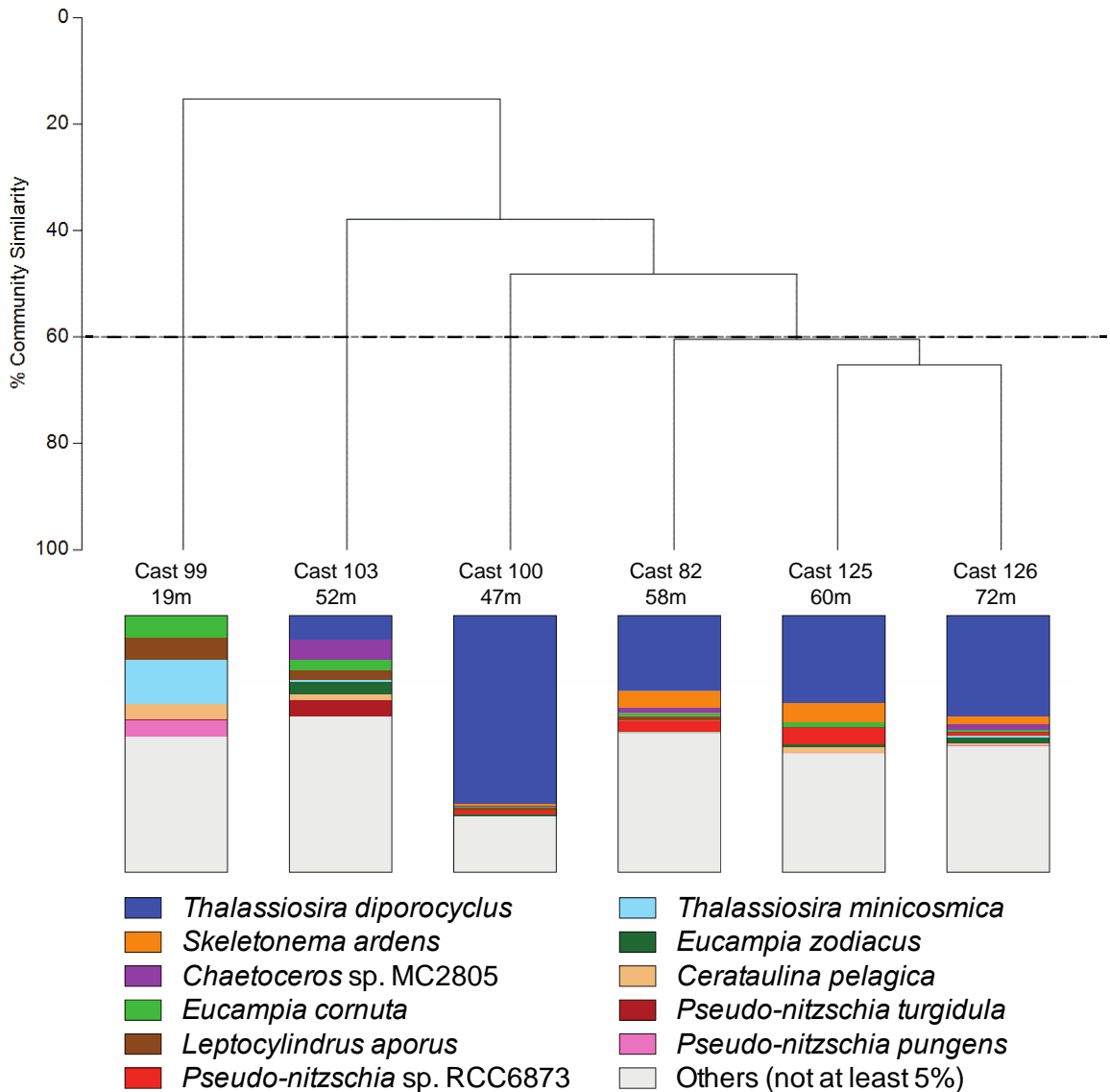


Fig. S5. Bray-Curtis similarity of the diatom 18S sequencing results from samples collected at the chlorophyll maximum (depth indicated below cast number) from a non-hotspot station on the shelf (Cast 99), a non-hotspot station on the slope (Cast 103), and 4 stations associated with the hotspot (Casts 82, 100, 125, and 126). The dashed line corresponds to 60% community similarity between samples. Before Bray-Curtis analysis, raw ASV count data was log-transformed. Below the dendrogram, the relative abundance of diatom species in each sample is shown. For graphing purposes, ASVs that were >99 % similar were grouped. Only diatoms that accounted for at least 5% of sequences at one of the stations are identified. The remaining diatom species are grouped in the “Others (not at least 5%)” category.

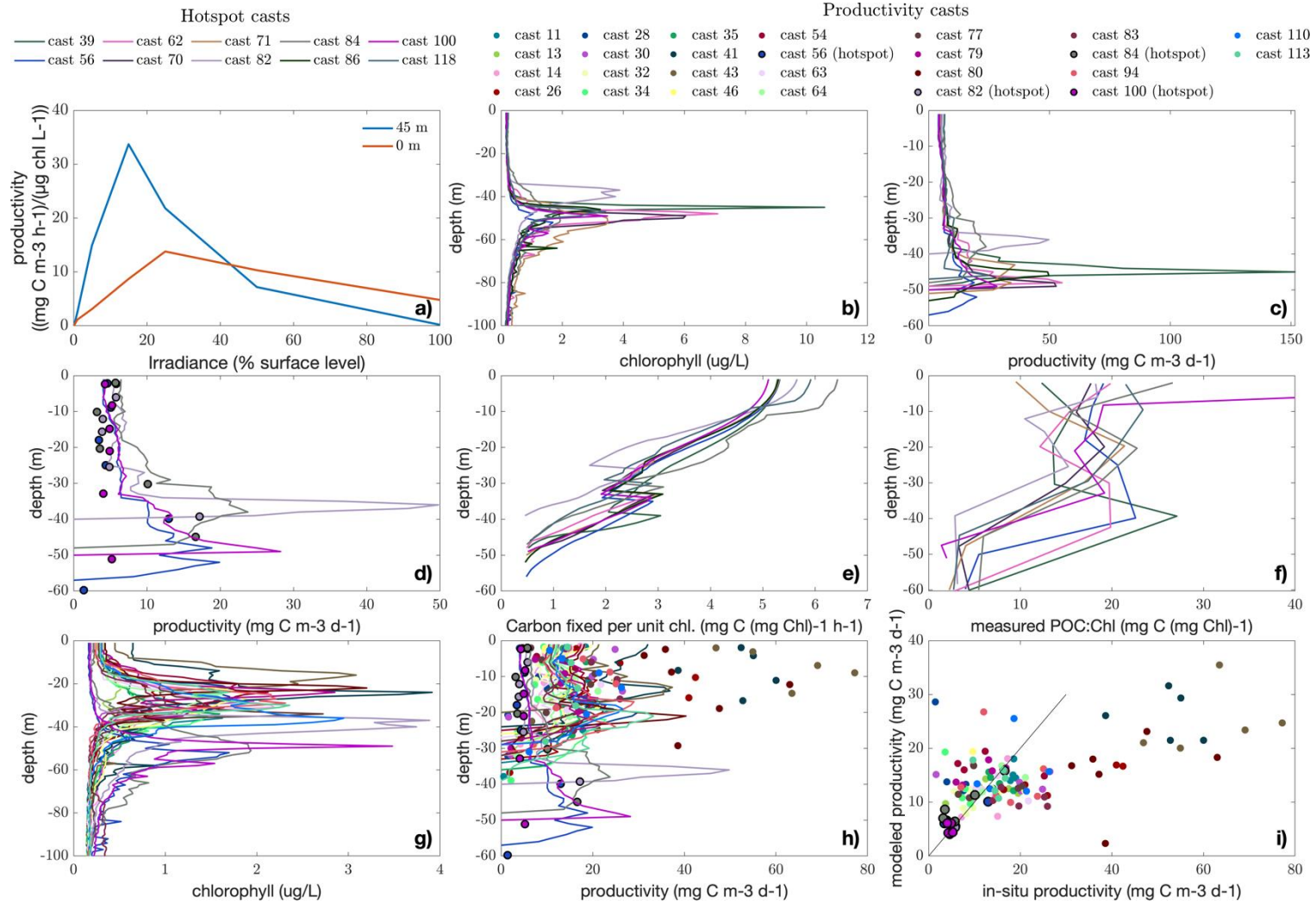


Fig. S6. Primary productivity: photosynthesis-irradiance experiments, from a bio-optical model, and measured *in situ*. a) Photosynthesis-irradiance experiment results from 45 m and 0 m at Station SLP (cast 100), chlorophyll-normalized; b) profiles of

chlorophyll *a* for hotspot casts derived from fluorescence measurements, c) bio-optical modeled productivity, down to the 1.3 $\mu\text{mol photons m}^{-2} \text{d}^{-1}$ isolume (the absolute compensation irradiance, Siegel et al., 2002); d) same as B, but only for casts for which *in situ* rates were measured, with in-situ rates shown as dots; e) profiles of modeled carbon fixed per unit chlorophyll down to the 1.3 $\mu\text{mol photons m}^{-2} \text{d}^{-1}$ isolume, with sharp transitions indicating the 100 $\mu\text{mol photons m}^{-2} \text{d}^{-1}$ isolume below which $E_k = 0.15 \times \text{surface PAR}$ ($E_k = 0.25 \times \text{surface PAR}$ above, see Text S8); f) ratio of POC (Fig. S3) to chlorophyll, showing high POC at many hotspot chlorophyll maxima, suggesting high concentrations of marine snow; g) profiles of chlorophyll for all primary productivity casts conducted during TN368; h) measured and modeled productivity for all TN368 productivity casts; i) measured vs. modeled productivity for all productivity casts, with black one-to-one line shown. Note the model underestimation of productivity at inner shelf stations 41, 43, and 80 (shown in Fig. S7).

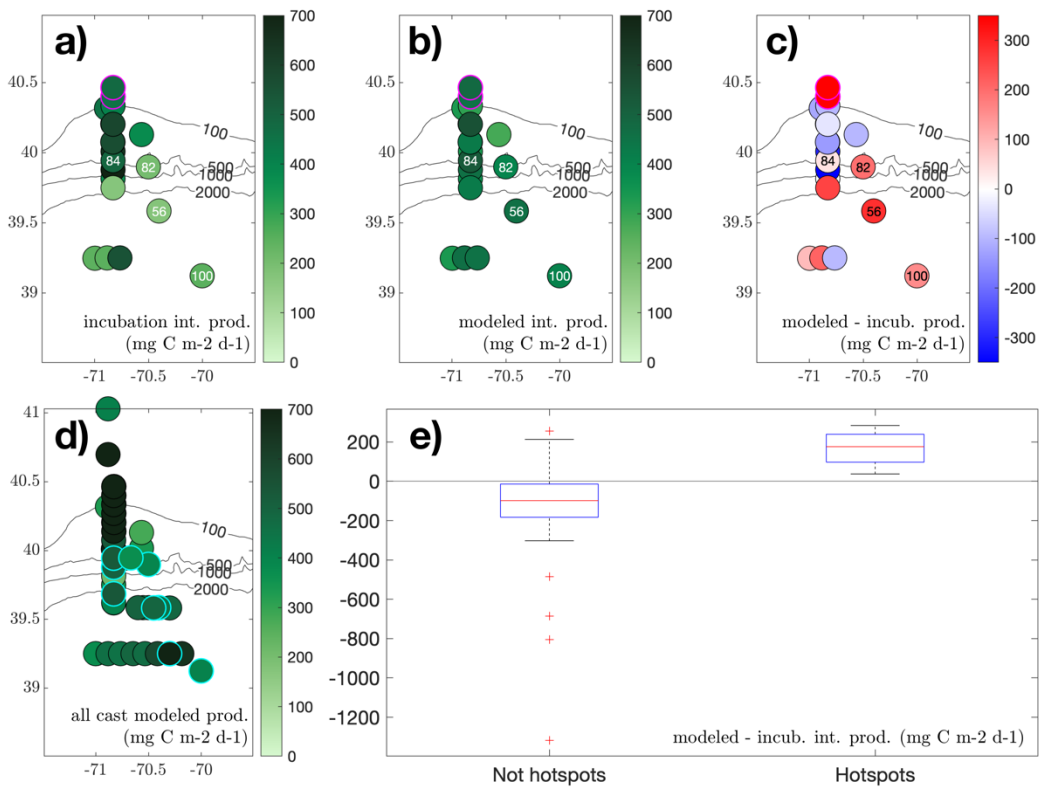


Fig. S7. Modeled and measured integrated primary productivity. A) Integrated primary productivity for all TN368 productivity incubation casts, with inner shelf stations 41, 43, and 80 highlighted in magenta, and hotspot casts labeled; B) modeled integrated primary productivity for the same set of casts; C) the difference between modeled and incubation productivity; D) modeled productivity for all TN368 casts, with hotspot casts highlighted in cyan; E) boxplot of the difference between modeled and incubation productivity, for non-hotspot and hotspot productivity casts.

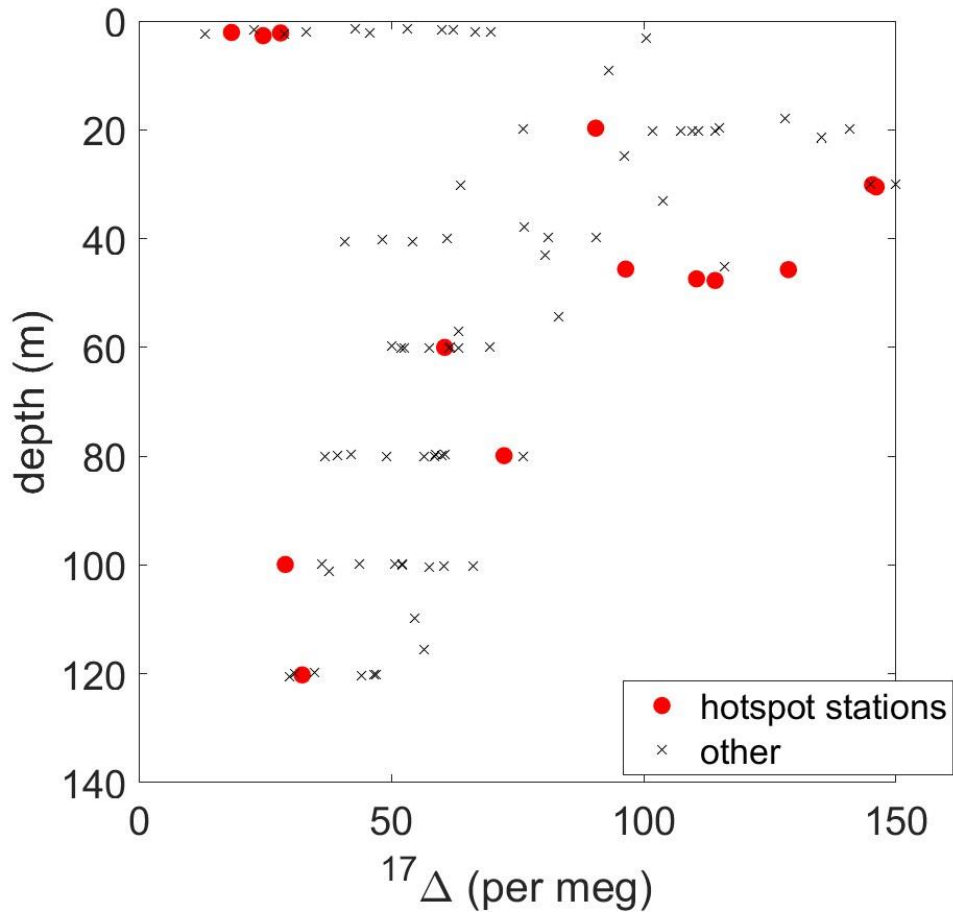


Fig. S8. Triple Oxygen Isotope signature, $^{17}\Delta$ (as defined in Text S9), of samples collected at stations designated as diatom hotspots (red circles) or other, non-hotspot stations (black x). A larger $^{17}\Delta$ means that a larger fraction of the dissolved oxygen present in the sample stems from photosynthesis as compared to atmospheric sources. Note that at the depths of the diatom hotspots (around 50 m), the samples in the hotspot stations have larger $^{17}\Delta$ and thus a higher fraction of photosynthetic oxygen than the most of the non-hotspot stations.

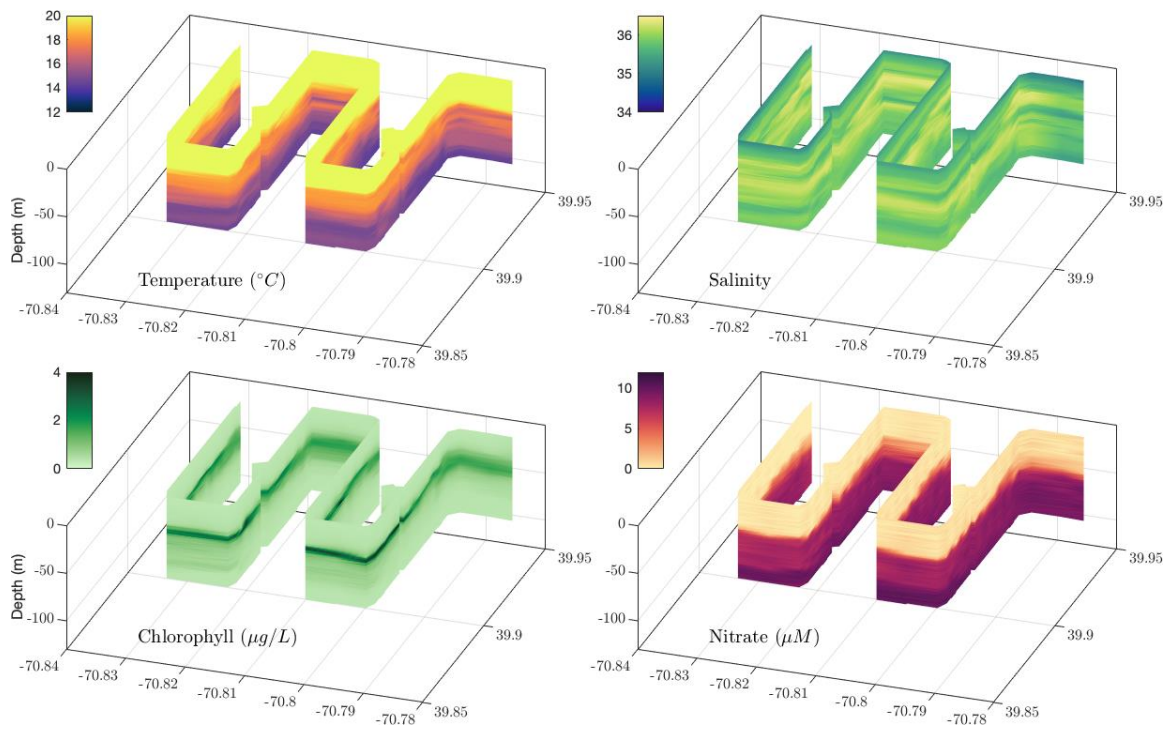


Fig. S9. REMUS 600 Mission 4A measurements of salinity, temperature, chlorophyll, and nitrate.

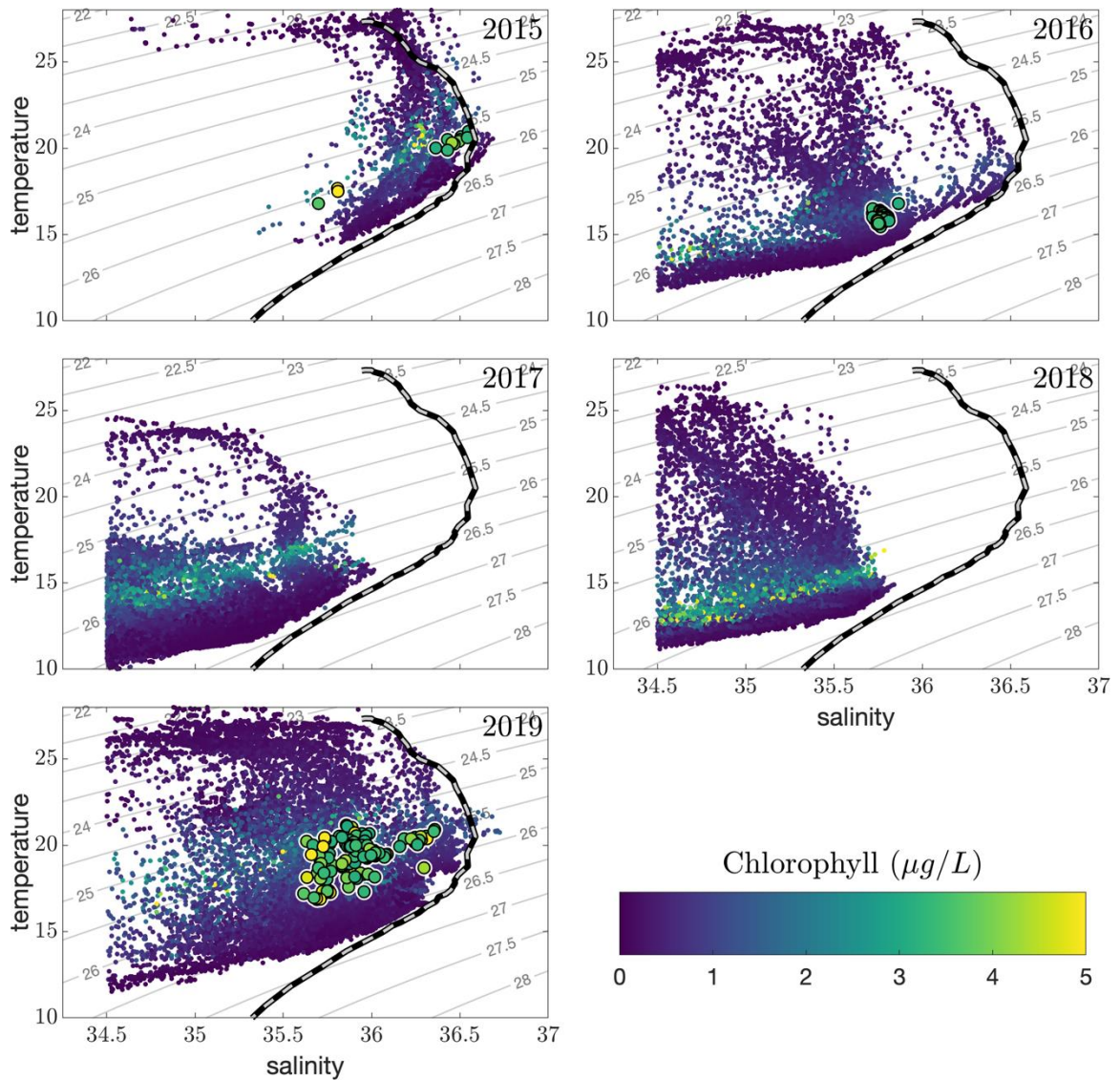


Fig. S10. OOI summer (June-August) slope sea glider measurements of temperature, salinity, and chlorophyll from 2015 – 2019. Large points show where 1) salinity > 35.6, 2) chlorophyll > $3 \mu\text{g/L}$, and 3) depth of the chlorophyll max between 40 and 60 m. Dashed black/white lines show Gulf Stream T-S profile from 69.5 E, 37 N from 1/10^o summer objectively analyzed climatological means from the National Centers for Environmental Information (NCEI) Northwest Atlantic Regional Ocean Climatology (Seidov, 2016).

Table S1. Classification categories, source of their training sets, and accuracy of the CNN classifications. The F1 score was calculated using 20% of the original CNN training withheld for evaluation purposes. Categories presented in this study are marked with an asterisk. AR29 is the March 2018 cruise of the R/V *Neil Armstrong* to the MAB, and TN368 is the July 2019 cruise of the R/V *Thomas G. Thompson*.

Category:	Training ROI Source:	F1 Score:
Bloom Conditions *	AR29	99%
Bubbles (Air) *	TN368	79%
<i>Ceratium</i> sp.	TN368	44%
Chaetognaths	TN368	81%
<i>Calanus finmarchicus</i>	TN368	52%
<i>Chaetoceros</i> sp. (combined with diatoms) *	TN368	12%
Copepods (small, unable to identify)	TN368	78%
<i>Coscinodiscus</i> sp. (combined with diatoms) *	TN368	86%
Decapod Larvae	TN368	57%
Diatoms (unidentified diatom chains) *	TN368	86%
Diatoms (Bloom, combined with diatoms) *	TN368	80%
Diatoms (Coils, mostly <i>Guinardia</i> sp., combined with diatoms) *	TN368	82%
Echinoderm Larvae	AR29	97%
Fecal Strings and Pellets	TN368	60%
<i>Foraminifera</i>	TN368	94%
Gelatinous Zooplankton	TN368	63%
Krill	TN368	0%
Krill Nauplii	TN368	78%
Larvaceans	TN368	79%
Marine Snow *	TN368	98%
<i>Oithona</i> sp. with visible egg sacs	TN368	25%
Out-of-Focus *	TN368	87%
<i>Phaeocystida</i> Protozoans	TN368	100%
<i>Pseudocalanus</i> sp. with visible egg sacs	TN368	67%
Pteropods	TN368	53%
Radiolarians	TN368	81%
Spherical Colonial Plankton (<i>Phaeocystis pouchetii</i>)	AR29	97%
<i>Thalassiosira diporocyclus</i> (combined with diatoms) *	TN368	86%
<i>Trichodesmium</i> sp.	TN368	62%
Unknown *	N/A	N/A

Table S2. Bio-optical modeled integrated productivity sensitivities and comparison with estimates of integrated productivity made with measurements made *in situ*

Cast #	Original modeled integrated productivity (g C m ⁻² d ⁻¹)	Upper k _d perturb. (g C m ⁻² d ⁻¹)	Chl <i>a</i> perturb. (g C m ⁻² d ⁻¹)	Absolute compensation irradi. perturb. (g C m ⁻² d ⁻¹)	Maximum perturb. (27 combinations in total) (g C m ⁻² d ⁻¹)	Uncertainty sum in quadrature (g C m ⁻² d ⁻¹)	Estimated prod. from <i>in situ</i> measurements (g C m ⁻² d ⁻¹)	Modeled productivity : measured productivity
39	0.7	± 0.2	< ± 0.05	< ± 0.05	± 0.3	± 0.2	-	-
56	0.5	± 0.2	< ± 0.05	< ± 0.05	± 0.2	± 0.2	0.2	2.6 ± 0.9
62	0.5	± 0.2	± 0.1	< ± 0.05	± 0.3	± 0.3	-	-
70	0.5	± 0.3	± 0.1	< ± 0.05	± 0.4	± 0.3	-	-
71	0.5	± 0.2	< ± 0.05	< ± 0.05	± 0.3	± 0.2	-	-
82	0.4	± 0.1	< ± 0.05	< ± 0.05	± 0.2	± 0.1	0.2	2.0 ± 1.0
84	0.5	± 0.1	< ± 0.05	< ± 0.05	± 0.1	± 0.1	0.5	1.1 ± 0.3
86	0.5	± 0.2	< ± 0.05	< ± 0.05	± 0.3	± 0.2	-	-
100	0.4	± 0.1	< ± 0.05	< ± 0.05	± 0.2	± 0.1	0.2	1.7 ± 0.5
118	0.3	± 0.1	< ± 0.05	< ± 0.05	± 0.2	± 0.2	-	-

Table S3. Parameters used in the biogeochemical model.

Symbol	Description	Value	Units
P_{max}	Phytoplankton max growth rate	3.0 ^a	day ⁻¹
α	Phytoplankton initial slope P-E curve	0.1 ^a	(W m ⁻²) ⁻¹ day ⁻¹
k_N	Phytoplankton nitrate uptake half-saturation	0.2	mmol N m ⁻³
k_{Si}	Phytoplankton silicate uptake half-saturation	0.2	mmol Si m ⁻³
R_{max}	Max grazing rate on phytoplankton	0.5	day ⁻¹
k_{phy}	Grazing on phytoplankton half-saturation	2.0	(mmol N m ⁻³) ²
k_p	Phytoplankton light attenuation coefficient	0.08 ^b	(mmol N) ⁻¹
R	Si:N ratio for phytoplankton uptake	$0.13 \times \frac{106}{16}$ ^c	mmol Si (mmol N) ⁻¹
γ_n	Excretion rate of nitrogen by zooplankton	0.1	dimensionless
σ_P	Mortality of phytoplankton	0.2	day ⁻¹
δ	Remineralization rate	0.05	day ⁻¹
ζ_d	Mortality of zooplankton	0.1	day ⁻¹
τ	Aggregation rate of phytoplankton and small detritus	0.01	(mmol N m ⁻³) ⁻¹ day ⁻¹
w_P	Sinking rate of phytoplankton	2.5	m day ⁻¹
w_{SD}	Sinking rate of small detritus	2.5	m day ⁻¹
w_{LD}	Sinking rate of large detritus	5.0	m day ⁻¹
β	Zooplankton assimilation efficiency	0.75	dimensionless

a. This study's bio-optical model.

b. Derived from TN368 CTD casts (see Text S10) and converted to (mmol N)⁻¹ by assuming a POC:Chl ratio of 50 and a C:N ratio of 106:16.

c. Brzezinski, (2004)

Dataset S1 (separate excel file). Details are provided for the read counts of ASVs in each of the samples used for DNA sequencing (Text S6).

References

- Altschul, S. F., Gish, W., Miller, W., Myers, E. W., & Lipman, D. J. (1990). Basic local alignment search tool. *Journal of Molecular Biology*, 215(3), 403–410. Retrieved from [https://doi.org/10.1016/S0022-2836\(05\)80360-2](https://doi.org/10.1016/S0022-2836(05)80360-2)
- Behrenfeld, M. J., & Falkowski, P. G. (1997a). A consumer's guide to phytoplankton primary productivity models. *Limnology and Oceanography*, 42(7), 1479–1491. <https://doi.org/10.4319/lo.1997.42.7.1479>
- Behrenfeld, M. J., & Falkowski, P. G. (1997b). Photosynthetic rates derived from satellite-based chlorophyll concentration. *Limnology and Oceanography*, 42(1), 1–20. <https://doi.org/10.4319/lo.1997.42.1.0001>
- Bray, J. R., & Curtis, J. T. (1957). An Ordination of the Upland Forest Communities of Southern Wisconsin. *Ecological Monographs*, 27(4), 325–349. <https://doi.org/10.2307/1942268>
- Brzezinski, M. A. (2004). The Si:C:N Ratio of Marine Diatoms: Interspecific Variability and the Effect of some Environmental Variables. *Journal of Phycology*, 21(3), 347–357. <https://doi.org/10.1111/j.0022-3646.1985.00347.x>
- Callahan, B. J., McMurdie, P. J., Rosen, M. J., Han, A. W., Johnson, A. J. A., & Holmes, S. P. (2016). DADA2: High-resolution sample inference from Illumina amplicon data. *Nature Methods*, 13(7), 581–583. <https://doi.org/10.1038/nmeth.3869>
- Chappell, P. D., Virginia Armbrust, E., Barbeau, K. A., Bundy, R. M., Moffett, J. W., Vedamati, J., & Jenkins, B. D. (2019). Patterns of diatom diversity correlate with dissolved trace metal concentrations and longitudinal position in the northeast Pacific coastal–offshore transition zone. *Marine Ecology Progress Series*, 609, 69–86. <https://doi.org/10.3354/meps12810>
- Clarke, K. R., & Gorley, R. N. (2018). Getting started with PRIMER v7. *Primer-E*, (1), 20. <https://doi.org/10.22201/ib.20078706e.2018.3.2409>
- Davis, C. S., Thwaites, F. T., Gallager, S. M., Hu, Q., Naiman, M., Sutton, T., et al. (2005). A three-axis fast-tow digital Video Plankton Recorder for rapid surveys of plankton taxa and hydrography. *Limnology and Oceanography: Methods*, 3, 59–74. <https://doi.org/10.4319/lom.2005.3.59>
- Fasham, M. J. R., Ducklow, H. W., & McKelvie, S. M. (1990). A nitrogen-based model of plankton dynamics in the ocean mixed layer. *Journal of Marine Research*, 48(3), 591–639.
- Fennel, K., Wilkin, J., Levin, J., Moisan, J., O'Reilly, J., & Haidvogel, D. (2006). Nitrogen cycling in the Middle Atlantic Bight: Results from a three-dimensional model and implications for the North Atlantic nitrogen budget. *Global Biogeochemical Cycles*, 20(3), 1–14. <https://doi.org/10.1029/2005GB002456>
- Friedrichs, M. A. M., Carr, M. E., Barber, R. T., Scardi, M., Antoine, D., Armstrong, R. A., et al. (2009). Assessing the uncertainties of model estimates of primary productivity in

- the tropical Pacific Ocean. *Journal of Marine Systems*, 76(1–2), 113–133.
<https://doi.org/10.1016/j.jmarsys.2008.05.010>
- Garcia, H., Weathers, K. W., Paver, C. R., Smolyar, I., Boyer, T. P., Locarnini, R. A., et al. (2019). World Ocean Atlas 2018. Vol. 4: Dissolved Inorganic Nutrients (phosphate, nitrate and nitrate+nitrite, silicate). *NOAA Atlas NESDIS 82*, 4(July), 35.
- González, P., Castaño, A., Peacock, E. E., Díez, J., del Coz, J. J., & Sosik, H. M. (2019). Automatic plankton quantification using deep features. *Journal of Plankton Research*, 41(4), 449–463. <https://doi.org/10.1093/plankt/fbz023>
- Hendricks, M. B., Bender, M. L., & Barnett, B. A. (2004). Net and gross O₂ production in the southern ocean from measurements of biological O₂ saturation and its triple isotope composition. *Deep-Sea Research Part I: Oceanographic Research Papers*, 51(11), 1541–1561. <https://doi.org/10.1016/j.dsr.2004.06.006>
- Holmes, R. M., Aminot, A., Kérouel, R., Hooker, B. A., & Peterson, B. J. (1999). A simple and precise method for measuring ammonium in marine and freshwater ecosystems. *Canadian Journal of Fisheries and Aquatic Sciences*, 56(10), 1801–1808.
<https://doi.org/10.1139/f99-128>
- Jassby, A. D., & Platt, T. (1976). Mathematical formulation of the relationship between photosynthesis and light for phytoplankton. *Limnology and Oceanography*, 21(4), 540–547. <https://doi.org/10.4319/lo.1976.21.4.0540>
- Joyce, T. M., Deser, C., & Spall, M. A. (2000). The relation between decadal variability of subtropical mode water and the North Atlantic Oscillation. *Journal of Climate*, 13(14), 2550–2569. [https://doi.org/10.1175/1520-0442\(2000\)013<2550:TRBDVO>2.0.CO;2](https://doi.org/10.1175/1520-0442(2000)013<2550:TRBDVO>2.0.CO;2)
- Juranek, L. W., & Quay, P. D. (2013). Using Triple Isotopes of Dissolved Oxygen to Evaluate Global Marine Productivity. *Annual Review of Marine Science*, 5(1), 503–524.
<https://doi.org/10.1146/annurev-marine-121211-172430>
- Kaiser, J. (2011). Technical note: Consistent calculation of aquatic gross production from oxygen triple isotope measurements. *Biogeosciences*, 8(7), 1793–1811.
<https://doi.org/10.5194/bg-8-1793-2011>
- Kalnay, E., Kanamitsu, M., Kistler, R., Collins, W., Deaven, D., Gandin, L., et al. (1996). The NCEP/NCAR 40-year reanalysis project. *Bulletin of the American Meteorological Society*, 77(3), 437–471.
- Luz, B., & Barkan, E. (2000). Assessment of oceanic productivity with the triple-isotope composition of dissolved oxygen. *Science*, 288(5473), 2028–2031.
<https://doi.org/10.1126/science.288.5473.2028>
- Luz, B., & Barkan, E. (2005). The isotopic ratios ¹⁷O/¹⁶O and ¹⁸O/¹⁶O in molecular oxygen and their significance in biogeochemistry. *Geochimica et Cosmochimica Acta*, 69(5), 1099–1110. <https://doi.org/10.1016/j.gca.2004.09.001>
- Martin, M. (2011). Cutadapt removes adapter sequences from high-throughput sequencing reads. *EMBnet Journal*, 17(1), 10. <https://doi.org/10.14806/ej.17.1.200>
- Moberg, E. A., & Sosik, H. M. (2012). Distance maps to estimate cell volume from two-dimensional plankton images. *Limnology and Oceanography: Methods*, 10(4), 278–288. <https://doi.org/10.4319/lom.2012.10.278>

- Morel, A. (1974). Optical properties of pure water and pure sea water. In *Optical Aspects of Oceanography* (pp. 1–24).
- Platt, T., & Jassby, A. D. (1976). The Relationship Between Photosynthesis and Light for Natural Assemblages of Coastal Marine Phytoplankton. *Journal of Phycology*, 12(4), 421–430. <https://doi.org/10.1111/j.1529-8817.1976.tb02866.x>
- Powell, T. M., Lewis, C. V. W. W., Curchitser, E. N., Haidvogel, D. B., Hermann, A. J., & Dobbins, E. L. (2006). Results from a three-dimensional, nested biological-physical model of the California Current System and comparisons with statistics from satellite imagery. *Journal of Geophysical Research: Oceans*, 111(7), 1–14. <https://doi.org/10.1029/2004JC002506>
- Prokopenko, M. G., Pauluis, O. M., Granger, J., & Yeung, L. Y. (2011). Exact evaluation of gross photosynthetic production from the oxygen triple-isotope composition of O₂: Implications for the net-to-gross primary production ratios. *Geophysical Research Letters*, 38(14), 1–5. <https://doi.org/10.1029/2011GL047652>
- Redfield, A. C. (1963). The influence of organisms on the composition of sea-water. *The Sea*, 26–77.
- Seidov, D. (2016). Northwest Atlantic Regional Climatology (NCEI Accession 0155889), 1–56. <https://doi.org/10.7289/V5RF5S2Q>
- Siegel, D. A., Doney, S. C., & Yoder, J. A. (2002). The North Atlantic spring phytoplankton bloom and Sverdrup's critical depth hypothesis. *Science*, 296(5568), 730–3. <https://doi.org/10.1126/science.1069174>
- Sosik, Heidi M., & Olson, R. J. (2007). Automated taxonomic classification of phytoplankton sampled with imaging-in-flow cytometry. *Limnology and Oceanography: Methods*, 5(6), 204–216. <https://doi.org/10.4319/lom.2007.5.204>
- Sosik, H.M., Peacock, E., & Santos, M. (2020). Abundance and biovolume of taxonomically-resolved phytoplankton and microzooplankton imaged continuously underway with an Imaging FlowCytobot along the NES-LTER Transect in winter 2018 ver 1. <https://doi.org/https://doi.org/10.6073/pasta/74775c4af51c237f2a20e4a8c011bc53>
- Stanley, R. H.R., Doney, S. C., Jenkins, W. J., & Lott, D. E. (2012). Apparent oxygen utilization rates calculated from tritium and helium-3 profiles at the Bermuda Atlantic Time-series Study site. *Biogeosciences*, 9(6), 1969–1983. <https://doi.org/10.5194/bg-9-1969-2012>
- Stanley, Rachel H.R., Kirkpatrick, J. B., Cassar, N., Barnett, B. A., & Bender, M. L. (2010). Net community production and gross primary production rates in the western equatorial Pacific. *Global Biogeochemical Cycles*, 24(4), 1–17. <https://doi.org/10.1029/2009GB003651>
- Zhang, W. G., & Partida, J. (2018). Frontal subduction of the Mid-Atlantic Bight Shelf Water at the onshore edge of a warm-core ring. *Journal of Geophysical Research: Oceans*, 123(11), 7795–7818. <https://doi.org/10.1029/2018JC013794>
- Zhang, W. G., McGillicuddy, D. J., & Gawarkiewicz, G. G. (2013). Is biological productivity enhanced at the New England shelfbreak front? *Journal of Geophysical Research: Oceans*, 118(1), 517–535. <https://doi.org/10.1002/jgrc.20068>

Zimmermann, J., Jahn, R., & Gemeinholzer, B. (2011). Barcoding diatoms: evaluation of the V4 subregion on the 18S rRNA gene, including new primers and protocols. *Organisms Diversity & Evolution*, 11(3), 173–192. <https://doi.org/10.1007/s13127-011-0050-6>